

F: LEFRJMR1 (JONSMOD2008)

Updated (June 09)

Influence of bottom frictional effects in sill regions
upon lee wave generation, and implications for
internal mixing

By

Jiuxing Xing and Alan M. Davies

Proudman Oceanographic Laboratory

6 Brownlow Street

Liverpool L3 5DA

England, U.K.

ABSTRACT

A cross sectional non-hydrostatic model using idealized sill topography is used to examine the influence of bottom friction upon unsteady lee wave generation and flow in the region of a sill. The implications of changes in shear and lee wave intensity in terms of local mixing are also considered. Motion is induced by a barotropic tidal flow which produces a hydraulic transition, associated with which are convective overturning cells, wave breaking and unsteady lee waves that give rise to mixing on the lee side of the sill. Calculations show that as bottom friction is increased current profiles on the shallow sill crest develop a highly sheared bottom boundary layer. This enhanced current shear changes the downwelling of isotherms downstream of the sill, with an associated increase in the hydraulic transition, wave breaking and convective mixing in the upper part of the water column. Both short and longer time calculations with wide and narrow sills for a number of sill depths and buoyancy frequencies confirm that increasing bottom friction modifies the flow and unsteady lee wave distribution on the downstream side of a sill. Associated with this increase in bottom friction coefficient there is increased mixing in the upper part of the water column with an associated decrease in the vertical temperature gradient. However this increase in mixing and decrease in temperature gradient in the upper part of the water column is very different from the conventional change in near bed temperature gradient produced by increased bottom mixing that occurs in shallow sea regions as the bottom drag coefficient is increased.

1. INTRODUCTION

In shallow sea regions with strong tidal currents, it is well known that bed stress, depending upon bottom roughness and tidal velocity, is the source of tidal turbulence in these areas. Since this turbulence is generated by bed roughness it is largest at the sea bed, and decreases with height above the bed. In essence mixing in the water column is generated at the bottom and diffuses up through the water column. In addition bed stress together with turbulence (parameterized by vertical eddy viscosity) are the features which determine tidal current profiles and tidal dissipation. Also tidally induced vertical mixing in the absence of wind forcing determines the rate at which solar heating is diffused from the surface layer to depth. In very shallow water with strong tidal mixing the water column remains well mixed, whereas in deeper water shelf sea regions a thermocline forms at depth producing a cold water bottom dome (e.g. Hill 1996, Hill et al. 1994, Xing and Davies 2005, Davies and Xing 2006). These cold water bottom domes are found in many shelf sea regions (e.g. Irish Sea and Yellow Sea, see Hill et al. 1994, Davies and Xing (2006)) where there are rapid increases in water depth and an associated decrease in tidal current amplitude and mixing.

In shelf edge regions where both the seasonal and permanent thermocline exist, and the topography is steep, then the on/off shelf motion of the tide gives rise to internal waves, as density surfaces are moved over the bottom slope (e.g. Baines 1995, Lamb 2004a, Legg et al. 2006, Gerkema et al. 2006, Cummins (2000) and Vlasenko et al. 2005). If the length scale of the topography is large compared with the tidal excursion length, then non-linear effects are small and an internal tide at the same frequency as the barotropic tide is produced (Gerkema and Zimmermann 1995). In this case the barotropic tide loses energy to the baroclinic tide, which subsequently propagates away from its generation region.

For the case in which the topographic length scale is comparable or shorter than the tidal excursion then non-linear effects are particularly important and energy cascades to

shorter wavelengths. In a hydrostatic model this build up of energy at the short wavelength in the shelf break region can produce instabilities. To stabilise these models horizontal diffusion is often increased in these regions (e.g. Willmott and Edwards 1987). If the hydrostatic approximation is not made (namely a non-hydrostatic model) then non-hydrostatic dispersion occurs and short waves (e.g. solitons, often observed at times of maximum tidal flow in shelf edge regions, unsteady lee waves (Nakamura et al. 2000, 2001, Stashuk et al. (2007), Vlasenko et al. (2002, 2005), Xing and Davies 2006, 2007, hereafter XD06, XD07) radiate energy from the region where non-linear effects are important. In this case energy cascades from the barotropic tide into short waves which give rise to mixing due to convective overturning or shear instabilities. The role of short (in the sense of less than the tidal excursion) scale topography (Gerkema and Zimmerman 1995) and non-linear effects (Lamb 2004a) in shelf slope regions in enhancing mixing in these areas with associated implications for ocean circulation is now well recognized (Samelson 1998, Spall 2001, Saenko 2006). In terms of oceanic mixing, calculations (Samelson 1998, Spall 2001, Saenko 2006) have shown that on long time scales (of order 40 years) enhanced mixing in the oceanic lateral boundary layer can influence circulation in the ocean interior which affects the meridional circulation.

Besides deep water shelf edge interactions between tides and topography in shallow water regions there is significant non-linear interaction at sill regions at the entrance to fjords (Stiegbrandt 1999, Stiegbrandt and Aure 1989, Vlasenko et al. 2002, Cummins 2000, Cummins et al. 2003) and lochs (Inall et al. 2004, 2005). In these areas flow over the sill is significant (of order in excess of 1 m s^{-1} , Inall et al. 2004) and hence the tidal excursion is appreciable compared to sill width. As shown in a range of measurements, analytical studies (e.g. Baines 1995) and numerical investigations (e.g. Vlasenko et al. 2002, XD06, Cummins 2000, Cummins et al. 2003) this gives rise to strong lee waves on the lee side of the sill as the

tide flows over it. Recent measurements in Loch Etive (Inall et al. 2004, 2005) and modelling using an idealized representation of a loch sill (XD06) demonstrated that these lee waves are responsible for a significant transfer of barotropic tidal energy into internal motion. This energy cascade from barotropic motion to internal waves that eventually break with resulting mixing, leads to an increase in the mixing that occurs on the lee side of the sill as the tide reverses (XD06). The importance of unsteady lee wave generation and propagation upon mixing in oceanic sea mount regions was recently demonstrated by Nakamura et al. 2000 and Nakamura and Awaji (2001). Consequently factors such as bottom friction which as will be shown influence across sill velocity shear, and the extent of unsteady lee wave generation and distribution on the lee side of a sill, influence temperature distributions in sill regions.

Analytical studies (e.g. Baines 1995) and numerical calculations (e.g. Vlasenko et al. 2002, XD06) show that as the tidal flow over the sill increases, lee waves are generated on the lee side of the sill. When the tidal velocity (U) in the sill region is such that it exceeds the first mode internal wave speed C_i , then the Froude number $F_r = U/C_i$ exceeds unity and the lee waves on the lee side are prevented from propagating back towards the sill and are amplified. When the tide reverses some of these lee waves are advected back towards the sill. As discussed by Davies and Xing (2007) (hereafter DX07) in the case of Loch Etive, for a realistic range of sill depths, vertical stratifications, and tidal forcings, unsteady lee waves formed on the lee side of the sill cannot propagate across the sill, and there is the potential for some of their energy to go into mixing. Consequently factors such as tidal forcing, sill width, depth, as shown by XD06 which influence the energy in the lee waves will affect the extent to which unsteady lee wave energy is available for mixing due to wave breaking (Nakamura et al. 2000, Nakamura and Awaji 2001). In essence unlike in a shallow sea where bottom friction produces mixing, it is the unsteady lee wave dissipation, convective overturning,

shear instabilities and internal wave breaking that are the source of mixing in sill regions. This mixing does not come from the lateral surface or bed boundary layers but is produced within the water column. As such it is “internal” rather than “external” mixing as defined by Van Haren and Howarth (2004). In view of this XD06, DX07 did not examine the role of bottom friction in determining the extent of unsteady lee wave generation, and hence the associated implications for mixing. Here the focus is upon the role of bottom friction upon internal wave mixing, in a cross section model. However in a three dimensional model it will also influence horizontal eddy formation and associated mixing.

The earlier work (XD06 DX07) was concerned exclusively with the Loch Etive region, with XD06 considering the influence of small scale topography on the sill of Loch Etive upon lee wave generation in this region. Subsequently this was extended to a more comprehensive study of how sill topography in general influenced the spectrum of internal wave generation in sill regions. To complement this work and the Loch Etive measurements, together with understanding how vertical stratification in the region of the Loch Etive sill influenced the lee wave response and flow separation downstream of the sill a detailed study of the role of stratification was performed (DX07).

In this paper that earlier work is extended by examining to what extent bottom friction influences the intensity of lee waves in the region of a sill. In essence the focus here is how bottom friction has the potential to influence mixing, not through differences in bed generated turbulence, but by its effect on unsteady lee waves, convective overturning and shear in the sill region. Initially calculations are performed with topography representing Loch Etive to determine how sensitive previous solutions in this region were to assumptions concerning bottom friction coefficient. Subsequently calculations are also performed with topography representing an idealized symmetric sill. In this case long term integrations are carried out to examine how bottom friction influences lee waves, internal tides and longer term mixing in a

more general context. In essence both the short term and long term influence of bottom friction upon mixing in different topographic contexts are examined.

The non-hydrostatic model and domain setup for Loch Etive are identical to XD06 and are described in Section 2. Subsequent sections deal with the influence of bottom frictional effects upon lee wave magnitude and temperature distributions in the sill region for the Loch Etive problem, and in the more general case, on both the shorter and longer time scale. A final section summarizes the main results of the study.

2. NUMERICAL MODEL

As previously (XD06) calculations were performed using the MIT code which is based on a z coordinate in the vertical. As details are given in Marshall et al. 1997, and its application to internal tide generation in Legg and Adcroft (2003), they will not be discussed here. The model integrates the three dimensional incompressible Boussinesq equations using either the hydrostatic approximation or the full non-hydrostatic equations, as applied here. As shown by XD07 it is essential to use a non-hydrostatic model to get the correct transfer of energy from the barotropic to the baroclinic flow in a sill region. Since the grid resolution used here is sufficiently fine to explicitly resolve the dominant mixing processes, subgrid scale mixing can be accurately approximated by constant values of horizontal and vertical eddy viscosity (A_h , A_v), and diffusivities (K_h , K_v). The implications of using a turbulence energy closure scheme are briefly discussed later.

All calculations were performed with the model in two dimensional (x , z) cross sectional form, initially with idealized topography and water depths representing the sill at the entrance to a Scottish Loch. In subsequent calculations (see later) a more idealized form of sill, namely a symmetric sill was used to ensure that conclusions drawn from the Loch Etive calculations were valid for a range of sill geometry. Also by performing longer term calculations with this topography, additional analysis of the importance of bottom friction

upon the energy cascade from the barotropic tide to the baroclinic tide, lee waves and high frequency motion could be examined.

Although a cross section slice model rather than a full three dimensional model is used here, a cross sectional model is appropriate in the region of a sill, where the lateral walls of the fjord constrain the flow to be over the sill. Considering initially the Loch Etive case, the sill width (of order 1000m), Loch length and water depths (of order 100m)(Fig. 1) approximated those of Loch Etive where recent measurements were made (Inall et al. 2004, 2005). As idealized topography and stratification were used no detailed comparison with Inall et al. 2004, 2005 can be made. However, as shown in XD06, DX07 the model can reproduce the train of unsteady lee waves that are found on the lee side of the sill, and the intensity and location of the jet that separates from the sill. The period and wavelength of the lee waves were in good agreement with that given by Inall et al. (2004, 2005). As comparison with Inall et al. (2004, 2005) is given in XD06 it will not be repeated here. In addition by using topography in the present calculations that is appropriate to Loch Etive the influence of bottom friction and hence bed types upon unsteady lee waves and the temperature field in the sill region can be assessed. However, to date no measurements of bed types on the top of the sill exist for validation purposes. Measurements in similar situations namely shallow banks in areas of strong tide flow have been made (Nash and Moum 2001) that suggest because of strong tidal currents, the sea bed on top of sills is very rough and hence there is a large drag coefficient. By using dimensions that are typical of sills at the entrance to lochs and fjords the resulting conclusions are relevant to modelling loch and fjord regions.

The idealized Loch Etive topography of the region (Fig 1) is characterized by a constant depth area at the left end of the domain ($h = 50$ m) with an open mouth at $x = -6500$ m, where M_2 barotropic tidal forcing is applied using a Flather type radiation condition. For

the baroclinic motion a flow relaxation zone is applied, with the temperature relaxed to its initial value. This is similar to the sponge layer used by Nakamura et al. (2000). Although not perfect this boundary condition is ideal in short term limited area calculations, but can cause some weak reflection in longer term calculations. The sill is situated at $x = 0$, with a water depth on top of the sill, namely $h_s = 15$ m, with water depths increasing to $h = 100$ m on the eastern side of the sill, which is closed at $x = 15000$ m. Initial conditions consisted of a horizontal uniform temperature field. The same initial vertical temperature gradient was used in all calculations to give a buoyancy frequencies (N). Initial conditions at time $t = 0$, of zero horizontal (u) and vertical (w) velocity were specified. Motion was induced by barotropic tidal forcing of the form

$$u = U_o \sin(\omega t)$$

at the western open boundary, where U_o is the specified amplitude of the tidal current, at the M_2 frequency ω . The Coriolis parameter f was fixed at $1.2 \times 10^{-4} \text{ s}^{-1}$, typical of northern latitude regions where fjord systems occur (Stieglbrandt (1999), Stieglbrandt and Aure (1989)). The application of a non zero value of f , gave rise to a bottom Ekman layer, although the cross sectional nature of the model meant that there was no cross channel variation in velocity. A fine uniform grid resolution $dz = 1$ m was used in the vertical with the horizontal grid gradually varying from $dx = 10$ m in the sill region to 100 m outside this area. This gave a model domain of 699×100 grid points and a time step $dt = 2.0$ s. With such a fine grid the coefficients of vertical and horizontal viscosity were set at $A_v = 10^{-3} \text{ m}^2 \text{ s}^{-1}$, $A_h = 10^{-1} \text{ m}^2 \text{ s}^{-1}$, with corresponding diffusivities of $K_v = K_h = 10^{-7} \text{ m}^2 \text{ s}^{-1}$. These coefficients were identical to those used in XD06, DX07 and yielded solutions for the unsteady lee wave distribution in good agreement with the Loch Etive measurements. For that reason the same values are used here.

A no heat flux boundary condition was applied at sea surface and sea bed, together with a zero surface stress condition. The form of the MIT code is such that there is a thin viscous boundary layer at the sea bed together with a quadratic friction law. By setting viscosity at the bed to K_V , the bed stress is in essence determined by the quadratic friction coefficient k when k is non-zero. When k is zero, the presence of the no slip condition at the bed, and non-zero K_V gives a small bed stress which produces a thin viscous boundary layer and hence the bed shear stress which is necessary for flow separation to occur on the lee side of the sill (Afanasyev and Peltier 2001, Lamb 2004b). The presence of this viscous layer and non-zero K_V together with quadratic friction leads to a reduction in velocity at the bed and a sheared water column above it, as found in tidal flows over sills. By adjusting the drag coefficient to simulate different bed types, the effect of bed stress and bottom shear on the flow and internal wave field can be examined. The calculations are therefore very different from the inviscid calculations of Afanasyev and Peltier (2001) or Lamb (2004b) which did not involve a drag law, or examine the influence of bed roughness. In essence a quadratic slip condition, is used here in the bed region, rather than a no-slip condition. However as vertical shear through the water column, particularly in the sill region is the important parameter that determines upper water column mixing, then similar results could be obtained with a no-slip bottom boundary condition.

In the calculations described here this quadratic friction law was used at the sea bed, with friction coefficient k varying from 0.0, 0.0025 to 0.025. By this means the effect of bottom skin friction varying from smooth through to very rough (gravel, small rocks) (Soulsby 1983) upon both bottom boundary layer mixing (external mixing) and internal mixing due to the hydraulic transition and lee waves could be examined.

3. NUMERICAL CALCULATIONS (Short period, Loch Etive Region)

In an initial series of short period calculations to examine the sensitivity of the solution to changes in bottom friction coefficient, the idealized Loch Eive topography (Fig. 1) and short term time integration used by XD06 was applied. By this means comparisons with earlier results (XD06) and observations in the region (Inall et al. 2004, 2005) could be made. As observations of Inall et al. 2004, 2005 were only made on the deeper water right hand side of the sill, the discussion will focus on this region. However, the physics of the hydraulic transition, unsteady lee wave generation, flow separation and shear induced mixing that occurs during the flood stage on the right hand side of the sill, also occurs on the left hand side during the ebb. In this case due to differences in water depth and sill slope their intensity is different although the processes generating them are the same. For this reason combined with the lack of observations and in order not to repeat arguments, in general only events on the right hand side of the sill will be discussed. As a detailed discussion of the physics of the flow over the sill is given in XD06, DX07, only the main features, in particular those influenced by bottom friction will be considered. In all calculations the topography and initial temperature field, giving a buoyancy frequency $N = 0.01 \text{ s}^{-1}$, together with tidal current amplitude $U_0 = 0.3 \text{ m s}^{-1}$ were used, although bottom friction coefficient k varied.

In an initial calculation $k = 0.0$ (Calc 1), motion was started from a state of rest by tidal forcing through the left open boundary. To examine the time variation of the flow and temperature field model output was produced at every 1/8 of a tidal cycle and selected output at this time interval is presented here. This tidal flow gives rise to an upwelling (Fig. 2a) of isotherms on the left side of the sill. As the current over the sill increases, the sill Froude number ($F_s = U_s/N h_s$), with h_s sill depth and U_s sill velocity increases and exceeds unity when U_s exceeds 15 cm s^{-1} . Thus the across sill velocity is super-critical for values exceeding 15 cm s^{-1} . On the right hand side of the sill, the water is deeper and the flow is sub-critical. As across sill flow changes from super-critical to sub-critical, the isotherms in

the upper part of the water column are depressed at $t = 2/8T$, where T is the tidal period (Fig. 2a). A near vertical isotherm is evident in the near bed layer on the right hand side of the sill at about $x = 500$ m.

The across sill velocity shows a maximum surface current of order 80 cm s^{-1} , in the upper 10 m of the water column, with a gradual reduction in the near bed region. Although the bed stress is small (see later discussion) it is non-zero and the flow is viscous, unlike the calculations of Afanasyev and Peltier (2001). Consequently as shown by Lamb (2004b) flow separation can occur. Although stress and viscous effects are the prime processes producing the separation, as shown by Klymak and Gegg (2003) internal pressure gradients arising from the vertical displacement of isotherms influence the location of the separation point, which in this case occurs at a depth of about 30 m. A narrow current jet leaves the sill at this position, and re-attaches at depth, with a second separation point and jet at 70 m (Fig. 2a).

Temperature contours in the surface layer show the presence of small scale ripples associated with the hydraulic jump. In addition temperature contour vertical separation increases. In essence this change in the vertical temperature gradient can occur by advection of water, or irreversible mixing (Peltier and Caulfield, 2003). As shown by the inviscid direct numerical simulations of Afanasyev and Peltier (2001) this can occur at about mid-water on the lee side of an obstacle. In the region where the current separates from the sill (the separation point) at a depth of about 60 m the isotherms separate due to the current “jet”. This enhances the temperature gradient below the “jet”, which together with the shear associated with the jet gives rise to a low Richardson number R_i (Fig. 3) in this region, where

$$R_i = \frac{-g}{\rho} \frac{\partial \rho}{\partial z} / \left(\left(\frac{\partial u}{\partial z} \right)^2 + \left(\frac{\partial v}{\partial z} \right)^2 \right),$$

where ρ is density. The presence of R_i numbers below the

critical value of 0.25 indicates a region where intense mixing can occur. Obviously the intensity of the mixing in a numerical model will depend upon the parameterization of the

diffusion. In the present model a small constant diffusion coefficient was used and hence mixing was reduced (see later). However as shown by Cummins (2000) in the POM hydrostatic ocean model where a Mellor and Yamada turbulence scheme was used, with a Richardson number dependent diffusion, the mixing can be large. Since the present model is non-hydrostatic, then density inversion can occur, giving rise to regions of negative R_i number (Fig. 3)

At $t = 4/8T$, half-way through the tidal cycle, the across sill barotropic velocity is near zero. However there is a small current jet on the right side of the sill (Fig. 2b). Within this jet is a flow to the right (+ve u velocity) with a region of negative u velocity above and below it. Associated with these flows is a downwelling of the temperature surfaces on the lee side of the sill in the upper part of the water column (Fig. 2b). At this time the intensity of the jet has increased as has the separation of the isotherms along the sill slope at about $z = -60$ m. This is in part due to advection into the region although at this time the current outside the jet is small. In addition mixing in the region (see later) can contribute to the widening of the isotherms at depth.

At $t = 8/8T$ (Fig. 2c) namely the end of the first tidal cycle the flow over the sill and on its right hand side is near zero. At this time there is no midwater jet, although there is some separation of the isotherms at $z = -60$ m. This separation occurs despite the absence of an appreciable flow, suggesting that mixing has taken place at this depth.

As the bottom friction coefficient is increased from $k = 0.0$ to 0.0025 to 0.025 the horizontal and vertical extent of the region of appreciable vertical displacements of the isotherms from their initial position is increased on the lee side of the sill (Fig. 2a). The position of the hydraulic transition at $x = 1000$ m ($t = 2/8T$, $k = 0.0025$ (Fig. 2a)) moves farther downstream to about $x = 1300$ m ($t = 2/8T$, $k = 0.025$, Fig. 2a). In addition there is an increase in the small scale vertical displacements of the isotherms between the sill top and the

location of the hydraulic transition. The space (of order 100m) and time scale (of order 10 mins) of these small scale waves suggests (see DX06, XD07 for more details) that they are unsteady lee waves formed on the downstream side of the sill. The formation of unsteady lee waves over steep topography such as that used here has been reported by Vlasenko et al. 2002, 2005, Stashchuk et al. 2007, Nakamura et al. 2000, 2001. This appears to be the primary cause of these waves which were also observed by Inall et al. (2004, 2005) on the lee side of Loch Etive. It is apparent from Figs. 2a,b that the intensity and spatial distribution of the temperature signal associated with the lee waves is significantly influenced by the value of k . In addition the strength of the current jet that separates from the downstream side of the sill at $t = 4/8T$ at about $x = 500$ m is also influenced by the choice of k . The value of k also influences where this jet separates from the sill and its downstream distribution (Fig. 2b). Even at slack water $t = 8/8T$ when the current is small the isotherm distribution at mid-water (Fig. 2c) has been influenced by the choice of k , suggesting that k has affected mid-water mixing (see later). A very different situation than in a shallow sea, where k influences bottom mixing.

To determine the reason for this it is valuable to examine how k influences the across sill flow. Time series of u current from $x = 0$ (crest of the sill) (Fig. 4a), for the second tidal cycle, shows flood tide (flow to the right) occurring at $t = 1.25T$, with slack water at $t = 1.5T$, and ebb-flow following this. As $k = 0.0$, and viscosity in the bottom boundary layer is small there is no evidence of significant shear in the bottom boundary layer during the tidal cycle.

Increasing the friction coefficient to $k = 0.0025$, a typical shallow sea value, corresponding to a sandy sea bed, leads to enhanced shear in the bottom boundary layer of the across sill velocity (Fig. 4b). A further increase to $k = 0.025$, the friction coefficient associated with large gravel or small boulders leads to enhanced shear in the near bed region (Fig. 4c). Although increasing k , leads to a reduction in near bed current and increase in

shear in the near bed region, depth mean current across the sill remain unchanged and hence the sill Froude number ($F_s = U/hN$) based on the initial N value remains constant in all calculations. On the lee side of the sill, this enhanced vertical shear in the flow increases convective overturning and associated breaking in the region of the hydraulic transition leading to enhanced vertical mixing (see later) on the lee side of the sill (Fig. 2a, $t = 2/8T$). Associated with this enhanced mixing is a reduction in N close to the top of the lee side of the sill. As shown by XD07, a local reduction in N in the region of the sill top leads to an enhancement in unsteady lee wave generation. Consequently unsteady lee waves can be readily generated in this region and are advected downstream (Fig. 2a). The presence of lee waves gives rise to the regions of enhanced u surface current as shown in Fig. 2a ($k = 0.0025$ and 0.025), and found in observations in Loch Etive (Inall et al. 2004, 2005). The convective overturning cells in the upper part of the water column give rise to low R_i numbers (Fig. 3, $k = 0.0025$ and 0.025) and enhanced surface mixing (see later). This is different to previously ($k = 0.0$) (Fig. 3) where shear at depth was the main source of mixing.

The change in the intensity of the unsteady lee waves and associated short waves on the downstream side of the sill at $x = 500$ m can be quantified in terms of time series over a tidal cycle of horizontal (u) and vertical (w) components of current associated with them (Fig. 5). Comparing time series of w shows (Fig. 5), that during flood tide, i.e. the first half of the tidal cycle, the magnitude and duration of the unsteady lee waves increases as k increases with an appreciable difference between $k = 0$ and $k = 0.0025$. As shown by DX07 the generation and intensity of unsteady lee waves is significantly influenced by the value of N near the sill crest on the downstream side of the sill. The fact that the lee wave signal has increased with increasing k , suggests that mixing has occurred on the lee side of the sill. This will be examined in terms of changes in N and discussed later. In addition changes in N due to mixing influence the frequency of the lee waves (XD07) Associated with the vertical

velocity due to the unsteady lee waves, are time variations of the u current which enhance or detract from the background tidal velocity giving rise to short period increases or decreases in u velocity during the flood stage of the tide. The nature of the mixed tidal-lee wave formed on the lee side of the sill, is that of a wave that is arrested at peak flood, that then propagates back toward the sill as tidal velocity decreases, with mixed tidal lee waves propagating out of the generation region (Nakamura et al 2000, Nakamura and Awaji 2001).

To examine how the energy transfer from the barotropic tide to the baroclinic tide, unsteady lee waves and other high frequency waves is influenced by the value of k , depth integrated power spectral density of the vertical velocity (see Legg and Huijts (2006), for details) were computed over the first two tidal cycles at $x = 1000$ m (Fig. 6). For the case of $k = 0$, there is more power in the low frequency (M_2 tide and its higher frequencies) end of the spectrum than in the high frequency end. However, for $k = 0.025$, the power in the internal tide in particular the higher harmonics is reduced, with a peak at about 70 to 80 times that of the M_2 tide, namely a period of 10 mins, corresponding to the unsteady lee wave period for the stratification used here (DX07). Short waves of this period on the lee side of Loch Etive were observed by Inall et al. (2004, 2005). For $k = 0.0025$ the spectrum (not shown) had a reduced tidal but increased high frequency power compared to $k = 0$. These power spectra clearly show that the distribution of baroclinic energy, during the first two tidal cycles between internal tides and high frequency short waves is influenced by the value of k .

To quantify the extent to which changes in k influence the mixing on the lee side of the sill, it is necessary to remove the contribution to the displacement of the isotherms by advection into a region. As shown by Legg and Huijts (2006) because of flow through the open boundary into the region it is difficult to perform an instantaneous budget for temperature advection. In addition because of isotherm overturning it is not possible to follow isotherms and accurately compute the volume change between them due to advection.

However, since it is the longer term change in stratification due to mixing that is important, and in a tidal flow the advective motion is sinusoidal, then the change in temperature due to irreversible mixing over a tidal cycle can be obtained by averaging the temperature field over a tidal cycle.

Contours of the tidally averaged (over the 3rd tidal cycle) temperature and density anomaly given as the difference between the tidally averaged buoyancy frequency (N^2) and its initial value (N_0^2) on the right hand side of the sill (in the region of the sill) are given in Fig. 7. In order to ensure that advection in the area of the open boundary does not influence the solution, it is important (as here) to ensure that the region of interest is well removed from the open boundary. Comparing temperature contours with their initial values (Fig. 1), and the change in N^2 , it is apparent that for $k = 0$ mid-water mixing has occurred on the lee side of the sill, with little change in the surface layer. The effect of the increase in mid-water mixing has been to slightly increase the stratification in the lower layer. As k is increased the extent of the region of mid-water mixing increases with some mixing occurring in the surface layer. As shown in DX07, changes in stratification on the upper half of the slope and in the surface layer on the lee side of a sill influence the magnitude and frequency of unsteady lee wave generation. This explains the differences in the lee waves found for various k values. Just how changes in the value of k influence mixing in the sill region and hence the spectrum of internal waves is difficult to determine. It is however clear from the calculations, that changes in k influence both the vertical shear and the internal jet, which affects mixing with associated changes in the internal wave field. It is evident from Figs. 7a,b that although there has been some change in stratification in the nearbed region due to bottom boundary layer mixing this is confined to the very near bed region and does not directly influence the mid-water mixing. This is very different than in a shallow sea region where bottom mixing determines mixing throughout the water column.

As time progresses mixing continues downstream of the sill (compare Figs. 7a and 7b (averaged over 4th tidal cycle)). In the case of $k = 0$, on this longer time scale there is some increase in mixing in the surface layer, with the region of mid-water mixing expanding slightly. A comparable expansion of the region of mid-water mixing occurs with $k = 0.0025$ (not shown) and $k = 0.025$.

The longer term effect of the mid-water mixing is to reduce the vertical and horizontal temperature gradient in the upper part of the water column in the region of the sill for all values of k . This suggests that without a river inflow from the upper part of the loch to maintain stratification in the sill region, as mixing occurs close to the sill, the distribution of energy between the internal tide and unsteady lee waves will change, as the stratification in the sill region evolves.

This change in energy can be quantified in terms of differences in power spectra based on the first two tidal cycles (Fig. 6) and second two tidal cycles (Fig. 8) at $x = 1000$ m, for $k = 0.0$ and 0.025 . It is evident for $k = 0.0$, that the M_2 internal tidal energy peak has increased, as has the energy at the unsteady lee wave period, with a decrease at the higher harmonics of the tide, between the third (Fig. 6) and fourth (Fig. 8) tidal cycle. For $k = 0.025$ there has been a small change in the low frequency end of the spectrum, with a reduction and broadening of the spectrum at the high frequency end.

These calculations suggest that although increasing k , as in a shallow sea region, leads to a small enhancement in bottom mixing this process has little or no effect upon internal mixing downstream from a sill. However, increasing k enhances the magnitude of the vertical shear in the near bed region of the flow over the sill, although its depth mean values and hence the sill Froude number are not affected by this change in k . This enhanced vertical shear in the flow increases convective overturning and associated breaking in the hydraulic transition region on the lee side of the sill. This leads to enhanced mixing on the lee side of

the sill near its top. As shown in DX07 increased mixing in this region, with an associated reduction in N , enhances unsteady lee wave generation. As this has been investigated in general in terms of the Froude number (see DX07, and references therein) it will not be elaborated here. In a tidal flow these unsteady lee waves are trapped on the lee side of the sill and amplified (XD06). When the tide reverses they can propagate towards the sill although as shown in XD06, DX07, for the sill heights considered here they do not propagate over the sill. Consequently they can enhance mixing on the lee side of the sill due to non-linear wave-wave interaction (Nakamura et al. 2000, 2001). Other forms of internal wave generated in the sill region e.g. internal tides, solitons etc. can propagate out of the region and in nature are responsible for mixing elsewhere.

As shown here changes in stratification in the sill region affects the partitioning of energy between the low frequency (baroclinic) part of the spectrum and the higher frequency part. In the absence of a river inflow to maintain stratification in the sill area, the region of mid-water mixing continues to grow. Although, even in a model, it is difficult to separate temperature changes due to diffusion from those due to advection, it is clear that the changes in internal wave energy spectrum from one tidal cycle to another, reflect changes in the density field due to mixing. On the longer term, in the case of $k = 0.0$, mixing in the upper part of the water column increases the lee wave energy in this region (not shown). However, for other k values the upper part of the water column becomes well mixed and the lee waves are mainly confined to the lower part of the water column. This shows that besides the lee wave generation and intensity of mixing depending upon the value of k , it is also influenced by time scale. To examine to what extent sill width and longer term mixing affects the role of bottom friction coefficient these calculations were repeated with a narrow sill.

4. NUMERICAL CALCULATIONS (longer period integration to a near steady state with a symmetric sill)

4.1 A narrow sill ($N = 1.0 \times 10^{-2} \text{ s}^{-1}$, $h_s = 15$ and 45 m)

In the previous calculations to be consistent with XD06, DX07, the sill topography was chosen to represent that of Loch Etive. In this section a symmetric narrow sill (Fig. 9), with sill half width a_s initially taken as a third of that used previously and subsequently a wider sill were considered. In addition in order to examine the long term effects of mixing in the sill region the calculation was performed for eight tidal cycles to reach a near steady state.

These longer term integrations with a narrow sill are essential to ensure that conclusions from the previous calculations are not specific to Loch Etive topography. Also by performing longer term integrations with symmetric sills of varying h_s , and sill width it is possible to examine additional physics such as form drag and power conversion that were not previously considered. As discussed previously since mixing in the sill region changes not only with the value of k , but also with time, and this influences lee wave generation which in turn affects mixing, it is important to examine long term solutions after identical integration periods. In such a long term calculation, in order to avoid false reflections from the lateral boundaries affecting mixing in the sill region, the domain was extended to $x = \pm 80\text{km}$. The sill was located at $x = 0$, with water depth at the sill (h_s) set at 15 m. Beyond the sill region water depth was fixed at $h = 100 \text{ m}$. Initial conditions were as in the Loch Etive calculations. In order to ensure that open boundary conditions did not influence the solution in the sill region the tide was applied as a body force in the momentum equation. Such forcing is appropriate in the present calculation since open boundaries are applied at each end of the domain and a symmetric sill is considered. The objective here was to examine response of internal waves and mixing to various parameters, e.g., N , h_s , a_s and k .

As the time history of the flow field is different to that described previously, the change in the velocity and temperature field as k is increased will be examined by comparing temperature and flow fields at the end of the first cycle (namely $t = 8/8T$) when the flow is a

maximum. This is comparable to $t = 2/8T$ in the previous Loch Etive calculations. However, as the objective is to examine mixing on the lee side of the sill for various values of k , this difference in tidal forcing is not important.

From Fig. 10a, it is apparent that there has been an appreciable change in the surface layer temperature field compared to the initial conditions, extending downstream as far as $x = 700$ m. As previously (Fig. 2a) the region of non-zero current velocity is restricted to the upper part of the water column. Contours of vertical velocity (not presented) show unsteady lee waves extending downstream from the sill. Richardson number contours (Fig. 11a) reveal a region of critical Richardson number, namely $R_i < 0.25$, where there is the potential for extensive mixing down stream of the sill. On the longer time scale, namely after seven tidal cycles, there is a substantial change in the distribution of surface isotherms, suggesting that mixing could have taken place in the upper part of the water column (Fig. 10b) on the lee side of the sill. Differences in the time averaged (over an M_2 tidal cycle) of the temperature and buoyancy frequency (not presented) compared with the initial ones shows a region of increased mixing above mid-water. On this longer time scale there is an appreciable unsteady lee wave signal in the upper part of the water column, and a significant vertical displacement of the isotherms on a space scale typical of lee waves.

As in the Loch Etive calculation, increasing the bottom friction coefficient to $k = 0.025$ changes the spatial distribution of the velocity and temperature field on the downstream side of the sill compared to $k = 0.0$ (Fig. 10b). Part of this is due to the fact that the maximum across sill velocity which occurs at the surface has slightly increased giving rise to increased downstream advection of the surface layer. In the case of $k = 0.025$, the region of convective overturning and appreciable unsteady lee wave activity extends farther downstream. In addition there is an increase in the vertical velocity (not presented) associated with the unsteady lee waves. This increase in unsteady lee wave activity with

increase in k is consistent with the results using the Loch Etive topography and leads to a modification of the region where $R_i < 0.25$ compared to the $k = 0.0$ solution (Fig. 11b).

The temperature distribution after seven tidal cycles (Fig. 11b) and the tidally averaged difference in temperature and buoyancy frequency (not presented) shows results consistent with those found in the Loch Etive case. Namely that increasing k , enhances mixing in the surface layer, with the downstream extent of this mixing increasing with increasing k . In addition on this longer time scale the vertical displacement of isotherms in the near bed region is reduced compared to that found with $k = 0.0$ (compare $k = 0.0$ and 0.025 temperature contours in Fig. 11b). Results using an intermediate k value, namely $k = 0.0025$ (not shown) were consistent with this and with the Loch Etive calculations. In essence in both the wide (Loch Etive) and narrow sill case increasing k enhances the downstream internal mixing.

To quantify the extent to which changes in k in the narrow sill case modify the frequency distribution of internal wave energy, power spectra at $x = 1000$ m for $k = 0$ and $k = 0.025$ were computed (Fig. 12). Comparing these spectra shows that in both cases there is a significant spectral peak at frequencies corresponding to unsteady lee waves. In addition this spectral peak is sharper than found in the Loch Etive calculation (compare Figs. 12 and 8) suggesting that as the sill narrows more power is transferred to unsteady lee waves for all values of k . However in the case of low k values there are peaks at the fundamental and higher harmonics of the tide, whereas at higher k values (e.g. $k = 0.025$) there is more of a continuum at low frequencies (Fig. 12).

In order to quantify the bottom friction effects on internal waves we compute internal motion induced form drag (F_D) and barotropic to baroclinic power conversion rate (R) in the region D extending to $x = \pm 500$ m (1500 m for a wide sill, see next section) on either side of the sill. The form drag can be written as

$$F_D = \frac{1}{D} \int_D P_b \frac{dh}{dx} dx$$

F_D is the force per unit area caused by internal wave induced horizontal pressure differences acting on opposite sides of the sill, with P_b the bottom pressure. Similarly the power conversion rate R can be obtained, as in Legg and Huijts (2006), from

$$R = \frac{1}{D} \int_D U_{bt} P_b \frac{dh}{dx} dx$$

with P_b given by

$$P_b = \rho_o g (\zeta - \zeta_{bt}) + P' (x, z_b, t)$$

where ζ is the free surface elevation, ζ_{bt} is the free surface elevation in a parallel barotropic calculation and $P' (x, z_b, t)$ is the fluctuating part of the bottom pressure field due to internal waves. In a non-hydrostatic calculation this accounts for pressure variations from both hydrostatic and non-hydrostatic processes.

Table 1 shows the time averaged (over an M_2 tidal cycle at the end of the model run) power conversion rate (R) for various model runs. It is evident that as k increases R decreases for all the cases. The main reason for this is due to the reduced vertical stratification as k increases. Another interesting feature is that R is much larger for the case of $h_s = 45m$ (a relatively deeper sill) than that of $h_s = 15m$, which is in contrast with recent work of small amplitude topography in the deep sea environment (Khatiwala 2003, Legg and Huijts 2006). The mechanism for this is out side the scope of the present paper.

4.2 A wide sill ($N = 1.0 \times 10^{-2} s^{-1}$, $h_s = 15 m$)

In order to determine how sill width influences the response to changing k , the previous series of calculations were repeated with a_s three times larger than the narrow sill calculation and k varying from low ($k = 0.00125$) to high ($k = 0.125$) (for some numerical

reasons the model is not stable with $k = 0$ for this topography) . The model domain, water depth, stratification and forcing were as before.

As previously for the narrow sill case (Fig. 10a) at $t = 8/8T$, the effect of increasing k , is to increase the downstream extent of the region of unsteady lee wave activity and associated convective overturning and mixing in the surface layer (Fig. 13a). Comparison of Figs. 10a and 13a, suggests that unsteady lee wave generation has been reduced by the decrease in sill aspect ratio as to be expected. Comparison of Richardson number contours (Fig. 14a) for $k = 0.00125$ and 0.025 as in the narrow sill case show that the region of critical Richardson number ($R_i < 0.25$) is significantly larger and closer to the surface for the higher k value.

As in the narrow sill case, on the longer time scale, namely after seven tidal cycles, temperature contours suggest that there is appreciably more mixing in the surface layer in the solution computed with the higher k value (Fig. 13b). This was confirmed as in the narrow sill case by differences in the time averaged temperature and buoyancy frequency (not presented). Similarly on this longer time scale the region of critical R_i number on the lee side of the sill computed with $k = 0.025$ is larger than that determined with the small k value.

To determine to what extent the change in sill width, and value of k influences the internal wave power density spectrum it was determined as previously (Fig. 12), at $x = 1000$ m for both values of k (Fig. 15). From a comparison of Figs. 12 and 15, it is evident that increasing the sill width has reduced the intensity of the spectral peak in the lee wave frequency band (Fig. 15) compared to previously (Fig. 12). However, as k is increased the power in the lee wave band is increased. These changes are consistent with those found for the Loch Etive and narrow sill calculations. These results, namely that increasing k , enhances the downstream extent of the region of mixing in the upper part of the water column are

consistent with those found in the narrow sill case and the calculations using idealized Loch Etive topography.

Time series over a tidal cycle at the end of the model run of form drag and power conversion rate show (Fig. 16) that as k is increased both form drag and power conversion rate decrease due to increasing energy going into mixing with a reduction of that available for baroclinic wave generation. This is consistent with the results based upon instantaneous and time averaged temperature and buoyancy comparisons, and power spectra plots.

4.3 *A wide sill ($N = 1.25 \times 10^{-2} \text{ s}^{-1}$, $h_s = 15 \text{ m}$)*

To determine if the previous conclusions are valid when the stratification is changed, the calculations were repeated with $N = 1.25 \times 10^{-2} \text{ s}^{-1}$. Results are illustrated in terms of velocity and temperature fields at $t = 56/8T$ and associated form drag and power conversion factor which indicates energy transfer from barotropic to baroclinic waves. Although increasing the vertical stratification for a given k tends to decrease the vertical mixing (compare Figs. 17 and 13b), it is apparent from Fig. 17 that mixing is increased as k is increased. Similarly, although the form drag and power conversion are increased by the increase in N (compare Figs. 16 and 18) (see also Table 1), these are reduced as k increases which is consistent with results from the earlier calculations.

4.4 *A wide sill ($N = 1.0 \times 10^{-2} \text{ s}^{-1}$, $h_s = 45 \text{ m}$)*

To determine if the previous conclusions in particular that the power conversion rate decreases as k increases, are valid in the case of a deeper sill, the earlier calculation was repeated with h_s increased to 45 m. Values of the tidally averaged conversion rate for the wide sill for a range of N and h_s values are given in Table 1 for three k values. From this table it is evident that even when N and h_s are increased, in all cases the power conversion

rate is reduced as k is increased. This confirms as in the initial idealized calculation using Loch Etive topography that upper water column mixing and the conversion of barotropic energy to baroclinic is influenced by the value of k .

5. CONCLUDING REMARKS

A non-hydrostatic model in cross sectional form has been used to examine the influence of bottom friction coefficient upon internal waves and “internal mixing” of tidal origin on the lee side of a sill. The work extends previous calculations, which showed that small scale topography on the lee side of the sill enhanced mixing (XD06). In addition it complements recent calculations (DX07) that showed that a reduction in buoyancy frequency on the lee side of a sill close to its top enhanced lee wave production with an associated increase in mixing down stream of the sill. This modelling work gives some insight into the processes that determine the enhanced mixing on the lee side of sills found in recent measurement campaigns (Farmer and Freeland 1983, Inall et al. 2004, 2005, Klymak and Gregg 2001, 2004, Nash and Moum 2001).

Initial calculations using topography representing Loch Etive, with the bottom friction coefficient $k = 0.0$, showed that downwelling occurred on the lee side of the sill, in response to across sill tidal flow. On the short time scale, of order a few hours, an hydraulic transition formed on the lee side of the sill, with associated convective overturning, wave breaking and mixing down stream of the sill. A current jet detached from the sill slope at depth, giving rise to shear and some mid-water mixing. As k was increased the across sill flow showed an increase in shear in the bottom boundary typical of a shallow sea region. However, the vertical extent of this sheared Ekman layer was confined to the near bed layer due to the small value of A_v used in the calculations.

The change in current shear in the vertical due to increasing k gave rise to a sharper hydraulic transition and enhanced (compared to $k = 0.0$) convective mixing downstream of

the sill. This enhanced convective mixing lead to a reduction in buoyancy on the lee side of the top of the sill. This had the effect of increasing the local Froude number on the lee side of the sill giving rise to increased unsteady lee wave and other short wave intensity on the downstream side of the sill. As discussed in DX07, these unsteady lee waves are trapped and amplified during the flood stage of the tide. During ebb they propagate back towards the sill where they enhance the mixing. Consequently the increase in unsteady lee wave amplitude and subsequent mixing, resulting from an increase in k leads to a cumulative increase in mixing. Other internal waves namely internal tides and mixed tidal-lee waves (Nakamura and Awaji (2001)) are not trapped and can propagate out of the region.

As k increases a frictional bottom boundary layer develops on the upper lee side of the sill associated with the current jet. However, below the position where the jet separates from the sill, and away from the sill the current is near zero and there is no bottom friction generated turbulence.

Calculations using a narrow symmetric sill, with the tide applied as a body force, show identical features as k is increased. In the case of a narrow sill, as discussed in XD07, stronger lee waves are generated than for a wide sill. A similar result was found here where for a given k lee waves from the narrow sill were stronger than those from the Loch Etive topography. On the short time scale namely first tidal period with a wide sill (e.g. Loch Etive) with $k = 0.0$, there is little or no unsteady lee waves, although with increased k lee waves are present. On the longer time scale, even with $k = 0.0$ unsteady lee waves are generated, and the intensity of these lee waves increases as sill width decreases.

Subsequent calculations performed with a wider symmetric sill, and a range of buoyancy frequencies N and sill depths h_s , showed that sill width, depth and buoyancy frequency influenced the mixing and power conversion to baroclinic motion. However, despite these changes calculations confirmed that independently of sill width and values of N

and h_s , mixing on the lee side of a sill increases as k increases. This is not due to bottom boundary layer turbulence as in a shallow sea region, but is due to the influence of k at the sill top upon the current profile in this region. As k is increased the vertical shear in across sill current increases giving rise to an increase in convective mixing and lee wave formation on the lee side of the sill, leading to a cumulative increase in mixing.

This suggests that not only do small scale topographic features on the upper part of the sill slope affect downstream mixing (XD06), but the roughness length and hence friction coefficient associated with the bed types (sand, gravel, rocks) will also influence the downstream mixing. Consequently measurement of bed types and small scale topography need to be made in sill regions. The fact that the downstream “internal mixing” persists for a long time and extends well beyond the topographic feature generating it explains the observations of mid-water mixing (Van Haren and Howarth 2004) often found in turbulence measurements in stratified regions, where the tidal bottom boundary layer is well below the observed feature.

Although the calculations performed here, were in terms of a cross sectional slice model, and therefore restricted to flows across sills where the flow is essentially normal to the sill, they will be appropriate in such a range of problems. However, in terms of full three-dimensional flow, there is the possibility of generating horizontal vortices which will increase the mixing above that found here. Such a study is beyond the scope of this paper, although the role of bottom friction upon vertical mixing should be comparable to that found here.

ACKNOWLEDGEMENTS

The authors are indebted to Mrs L Parry and E. Ashton for preparing the text.

REFERENCES

- Afanasyev, Y.D. and W.R. Peltier (2001) On breaking internal waves over the sill in Knight Inlet. *Proceedings of the Royal Society London*, A457, 2799-2825.
- Baines, P.G. (1995) *Topographic effects on stratified flows*. Cambridge Monographs on Mechanics. Cambridge University Press.
- Cummins, P.F. (2000) Stratified flow over topography: time-dependent comparisons between model solutions and observations. *Dynamic Atmospheric Oceans*, 33, 43-72.
- Cummins, P.F., S. Vagle, L. Armi and D.M. Farmer (2003) Stratified flow over topography: upstream influence and generation of non-linear internal waves. *Proceedings of Royal Society of London*, A459, 1467-1487.
- Davies, A.M. and Xing, J. (2006) Effect of topography and mixing parameterization upon the circulation in cold water domes. *Journal of Geophysical Research*, 111, C03018, doi:10.1029/2005JC003066.
- Davies, A.M. and J. Xing (2007) On the influence of stratification and tidal forcing upon mixing in sill regions. *Ocean Dynamics*, 57, 431-451.
- Edwards, K.A., P. MacCready, J.N. Moum, G. Pawlak, J.M. Klymak and A. Perlin (2004) Form drag and mixing due to tidal flow past a sharp point. *Journal of Physical Oceanography*, 34, 1297-1312.
- Farmer, D.M. and H.J. Freeland (1983) *The Physical Oceanography of Fjords*. *Progress in Oceanography*, 12, 147-220.
- Gerkema, T. and J.T.F. Zimmerman (1995) Generation of non-linear internal tides and solitary waves. *Journal of Physical Oceanography*, 25, 1081-1094.
- Gerkema, T., C. Staquet and P. Bouruet-Aubertot (2006) Non-linear effects in internal-tide beams and mixing. *Ocean Modelling*, 12, 302-318.

- Hill, A.E., Durazo, R. and Smeed, D.A. (1994) Observations of a cyclonic gyre in the western Irish Sea. *Continental Shelf Research*, 14, 479-490.
- Hill, A.E. (1996) Spin-down and the dynamics of dense pool gyres in shallow seas. *Journal of Marine Research*, 54, 471-486.
- Inall, M.E., F.R. Cottier, C. Griffiths and T.P. Rippeth (2004) Sill dynamics and energy transformation in a jet fjord. *Ocean Dynamics*, 54, 307-314.
- Inall, M.E., T.P. Rippeth, C. Griffiths and P. Wiles (2005) Evolution and distribution of TKE production and dissipation within stratified flow over topography. *Geophys. Res. Lett.*, 32, L08607, doi:10.1029/2004GL022289.
- Khatiwala, S. (2003) Generation of internal tides in an ocean of finite depth: analytical and numerical calculations. *Deep Sea Res.* 50, 3-21.
- Klymak, J.M. and M.C. Gregg (2001) Three-dimensional nature of flow near a sill. *Journal of Geophysical Research*, 106, 22,295-22,311.
- Klymak, J.M. and M.C. Gregg (2003) The role of upstream waves and a downstream density pool in the growth of lee waves: stratified flow over the Knight Inlet sill. *Journal of Physical Oceanography*, 33, 1446-1461.
- Klymak, J.M. and M.C. Gregg (2004) Tidally generated turbulence over the Knight Inlet Sill, *Journal of Physical Oceanography*, 34, 1135-1151.
- Lamb, K.G. (2004a) Non-linear interaction among internal wave beams generated by tidal flow over supercritical topography. *Geophysical Research Letters*, 31, L09313, doi:10.1029/2003GL019393.
- Lamb, K.G. (2004b) On boundary-layer separation and internal wave generation at the Knight Inlet sill. *Proceedings of the Royal Society London*, A460, 2305-2337.
- Legg, S. and A. Adcroft (2003) Internal wave breaking at concave and convex continental slopes. *Journal of Physical Oceanography*, 33, 2224-2246.

- Legg, S., K.M.H. Huijts (2006) Preliminary simulations of internal waves and mixing generated by finite amplitude tidal flow over isolated topography. *Deep Sea Research*, 53, 140-156.
- Marshall, J., C. Hill, L. Perelman and A. Adcroft (1997) Hydrostatic, quasi-hydrostatic and non-hydrostatic ocean modelling. *J. Geophys. Res.*, 102, 5733-5752.
- Moum, J.N., J.M. Klymak, J.D. Nash, A. Perlin and W.D. Smyth (2007) Energy transport by non-linear internal waves. *Journal of Physical Oceanography*, 37, 1968-1988.
- Nakamura, T., T. Awaji, T. Hatayama and K. Akitomo (2000) The generation of large-amplitude unsteady lee waves by sub-inertial K_1 tidal flow: A possible vertical mixing mechanism in the Kuril Straits. *Journal of Physical Oceanography*, 30, 1601-1621.
- Nakamura, T. and T. Awaji (2001) A growth mechanism for topographic internal waves generated by an oscillatory flow. *Journal of Physical Oceanography*, 31, 2511-2524.
- Nash, J.D., J.N. Moum (2001) Internal hydraulic flows on the continental shelf: High drag states over a small bank. *Journal Geophysical Research*, 106(C3), 4593-4612, 10.1029/1999JC000183.
- Peltier, W.R. and C.P. Caulfield (2003) Mixing efficiency in stratified shear flows. *Annual Reviews in Fluid Mechanics*, 35, 135-167.
- Saenko, O.A. (2006) The effect of localized mixing on the Ocean Circulation and time-dependent climate change. *Journal of Physical Oceanography*, 36, 140-160.
- Samelson, R.M. (1998) Large scale circulation with locally enhanced vertical mixing. *Journal of Physical Oceanography*, 28, 712-726.
- Soulsby, R. L. (1983) The bottom boundary layer of shelf seas, pg 189-262 in *Physical Oceanography of Coastal and Shelf Sea*, ed. B. Johns.

- Spall, M.A. (2001) Large scale circulations forced by localized mixing over a sloping bottom. *Journal of Physical Oceanography*, 31, 2369-2384.
- Stashchuk, N., M. Inall and V. Vlasenko (2007) Analysis of supercritical stratified tidal flow in a Scottish Fjord. *Journal of Physical oceanography*, 37, 1793-1810.
- Stigebrandt, A. and J. Aure (1989) Vertical mixing in basin waters of fjords. *Journal of Physical Oceanography*, 19, 917-926.
- Stigebrandt, A. (1999) Resistance to barotropic tidal flow in straits by baroclinic wave drag. *Journal of Physical Oceanography*, 29, 191-197.
- Van Haren, H., L. Mass, J.T.F. Zimmerman, H. Ridderinkhof and H. Malschaert (1999) Strong inertial currents and marginal internal wave stability in the central North Sea. *Geophysical Research Letters*, 26, 2993-2996.
- Van Haren, H. and J. Howarth (2004) Enhanced stability during reduction of stratification in the North Sea. *Continental Shelf Research*, 24, 805-819.
- Venayagamoorthy, S.K., O.B. Fringer (2005) Non-hydrostatic and non-linear contributions to the energy flux budget in non-linear internal waves. *Geophysical Research Letters*, 32, L15603, doi:10.1029/2005GL023432.
- Vlasenko, V., Stashchuk, N. and Hutter, K. (2005) Baroclinic tides. Theoretical modelling and observational evidence. Cambridge University Press.
- Vlasenko, V. Stashchuk, N. and Hutter, K. (2002) Water exchange in fjords induced by tidally generated internal lee waves. *Dynamics of Atmospheres and Oceans*, 35(1), 63-83.
- Willmott, A. and Edwards, P.A. (1987) A numerical model for the generation of tidally forced non-linear waves over topography. *Continental Shelf Research*, 7, 457-484.
- Xing, J. and A.M. Davies (2005) Influence of a cold water bottom dome on internal wave trapping. *Geophysical Research Letters*, 32, L03601, doi:10.1029/2004GL021833.

Xing, J. and A.M. Davies (2006) Processes influencing tidal mixing in the region of sills. Geophysical Research Letters, 33, L04603,doi:10.1029/2005GL025226.

Xing, J. and A.M. Davies (2007) On the importance of non-hydrostatic processes in determining tidally induced mixing in sill regions. Continental Shelf Research, 27, 2162-2185.

FIGURE CAPTIONS

- Fig. 1: Idealized topography used in the Loch Etive calculation, with initial temperature (T) distribution ($^{\circ}\text{C}$, contour interval c.i. = 0.5°C), and location of sill at $x = 0$, with an open boundary on the left side and closed boundary at the right.
- Fig. 2a: Sub-domain of the region, showing temperature field ($^{\circ}\text{C}$, c.i. = 0.25°C), u velocity (cm s^{-1}), computed with $k = 0.0, 0.0025$ and 0.025 at $t = 2/8T$, where T is the tidal period.
- Fig. 2b: As Fig. 2a, but at $t = 4/8T$.
- Fig. 2c: As Fig. 2a, but at $t = 8/8T$.
- Fig. 3: Richardson Number (R_i) and temperature contours (c.i. = 0.5°C) distribution at $t = 2/8T$ on the right hand side of the sill (note: only shading area of $R_i < 0.25$, also negative R_i (darker colour) showing static unstable regions).
- Fig. 4: Time series of u (c.i. = 5 cm s^{-1}) at $x = 0$ (centre of sill) over the second tidal cycle (note solid contour positive and dashed contour negative) computed with (a) $k = 0.0$, (b) $k = 0.0025$ and (c) $k = 0.025$.
- Fig. 5: Time series of u (top) and vertical velocity w (bottom) at $x = 500 \text{ m}$ computed with (a) $k = 0.0$, (b) $k = 0.0025$ and (c) $k = 0.025$.
- Fig. 6: Depth integrated power spectral density of vertical velocity w at frequencies normalized with respect to the M_2 tide at $x = 1000 \text{ m}$, computed over first two tidal cycles with (a) $k = 0.0$ and (b) $k = 0.025$.
- Fig. 7a: Tidally averaged density stratification anomaly ($\overline{N^2} - N_0^2$) where $\overline{N^2}$ is buoyancy frequency from the temperature field averaged over the third tidal cycle and N_0^2 its initial value. Also shown are temperature contours averaged over the third tidal cycle, computed with (a) $k = 0.0$ and (b) $k = 0.025$.
- Fig. 7b: As Fig. 7a but averaged over the fourth tidal cycle.

Fig. 8: As Fig. 6 but over second two tidal cycles.

Fig. 9: Idealized topography showing location of narrow sill and initial temperature (T) distribution ($^{\circ}\text{C}$, contour interval c.i. = 0.5°C).

Fig. 10a: Sub-domain of the region close to the sill, showing temperature field ($^{\circ}\text{C}$, contour interval, c.i. = 0.5°C , u velocity (cm s^{-1}), computed with $k = 0.0$ and $k = 0.025$ at $t = 8/8T$, where T is the tidal period.

Fig. 10b: As Fig. 10a, but at $t = 56/8T$.

Fig. 11a: As Fig. 3, but for narrow sill with $k = 0.0$, and 0.025 at $t = 8/8T$.

Fig. 11b: As Fig. 11a, but at $t = 56/8T$.

Fig. 12: As Fig. 6, but computed with the narrow sill.

Fig. 13a: Sub-domain of the region close to the sill, showing temperature field ($^{\circ}\text{C}$, c.i. = 0.5°C , u velocity (cm s^{-1}), computed using the idealized wide sill and $N = 1.0 \times 10^{-2} \text{ s}^{-1}$, with $k = 0.00125$ and $k = 0.025$ at $t = 8/8T$, where T is the tidal period.

Fig. 13b: As Fig. 13a, but at $t = 56/8T$.

Fig. 14a: As Fig. 3, but for an idealized wide sill and $N = 1.0 \times 10^{-2} \text{ s}^{-1}$ with $k = 0.00125$ and 0.025 at $t = 8/8T$.

Fig. 14b: As Fig. 14a, but at $t = 56/8T$.

Fig. 15: As Fig. 6, but computed with an idealized wide sill and $N = 1.0 \times 10^{-2} \text{ s}^{-1}$ with $k = 0.00125$ and 0.0125 .

Fig. 16: Time series over a tidal cycle of form drag (Pa) and power conversion rate (W m^{-2}) for $k = 0.00125$ (solid line) and $k = 0.025$ (dashed line) computed with the idealized wide sill with $N = 1.0 \times 10^{-2} \text{ s}^{-1}$.

Fig. 17: As Fig. 14b, but with $N = 1.25 \times 10^{-2} \text{ s}^{-1}$.

Fig. 18: As Fig. 16, but with $N = 1.5 \times 10^{-2} \text{ s}^{-1}$.

TABLE 1: Values of time averaged (over an M_2 tidal cycle) power conversion rate (W/m^2) for a range of N and h_s values, as a function of k for a narrow and wide sill

k	Narrow sill $N=0.01\ s^{-1}$ $h_s = 15\ m$	Narrow sill $N=0.01\ s^{-1}$ $h_s = 45\ m$	Wide sill $N = 0.01\ s^{-1}$ $h_s = 15\ m$	Wide sill $N=0.01\ s^{-1}$ $h_s = 45\ m$	Wide sill $N = 0.0125\ s^{-1}$ $h_s = 15\ m$
0.00125 (0.0 for narrow)	0.093	0.214	0.039	0.079	0.065
0.0025	0.085	0.208	0.031	0.074	0.049
0.025	0.054	0.191	0.020	0.057	0.037

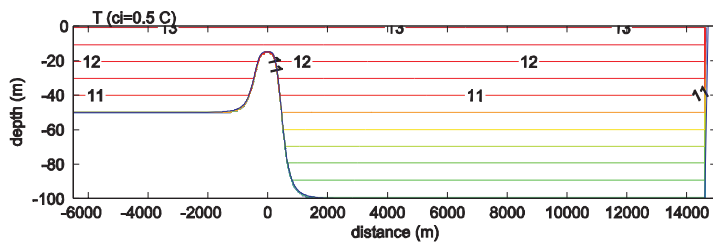


Fig.1

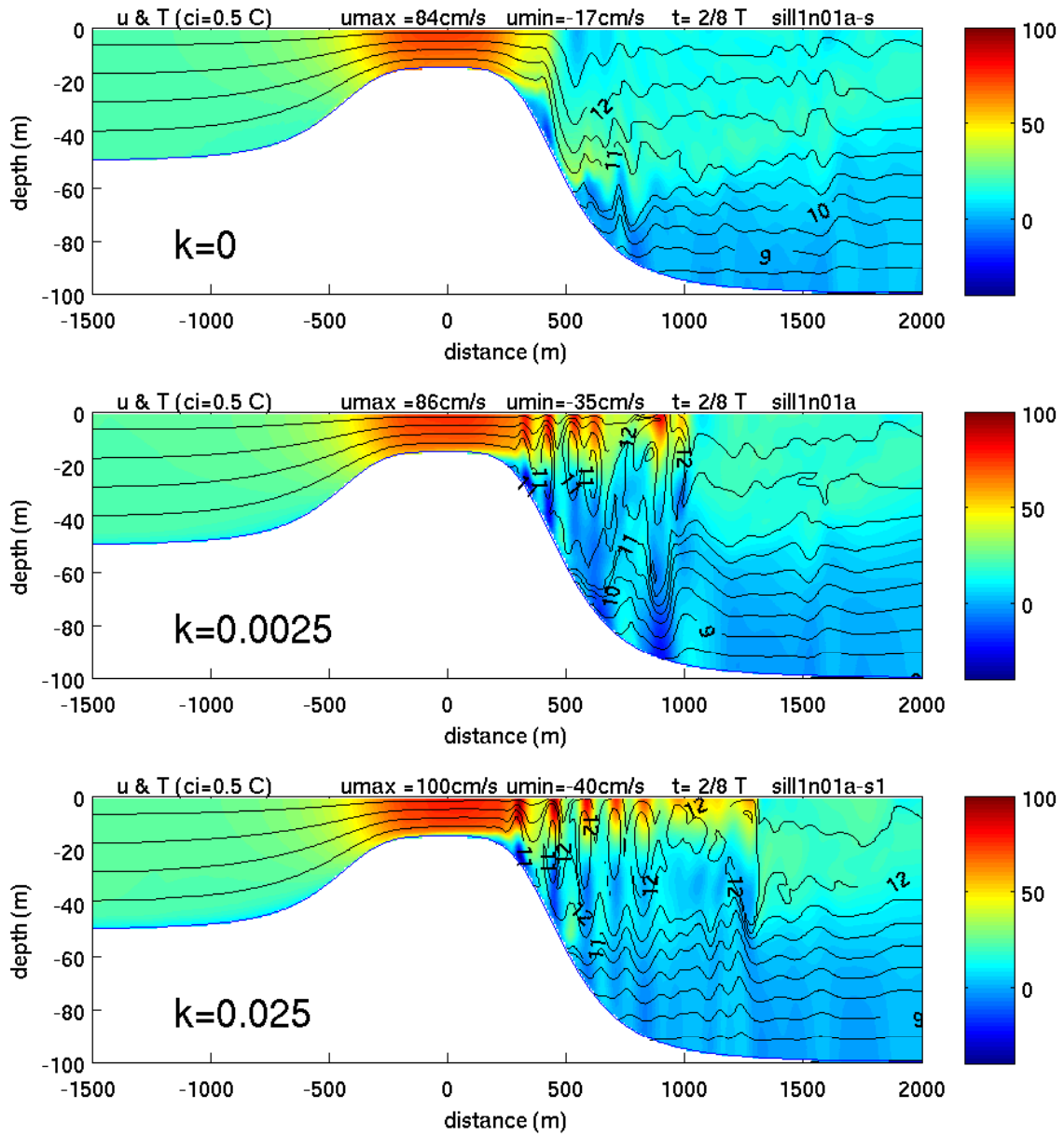


Fig. 2a

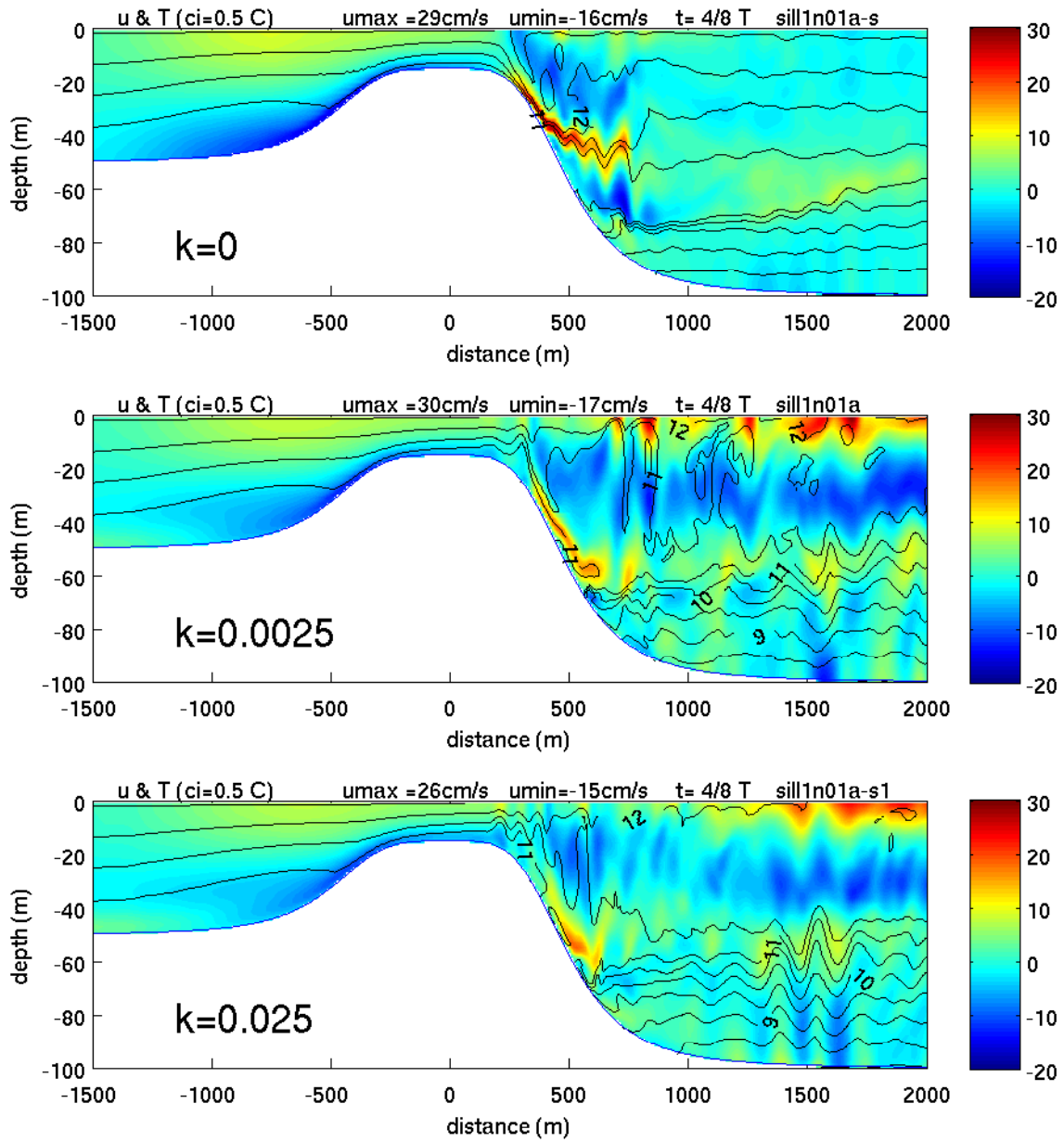


Fig. 2b

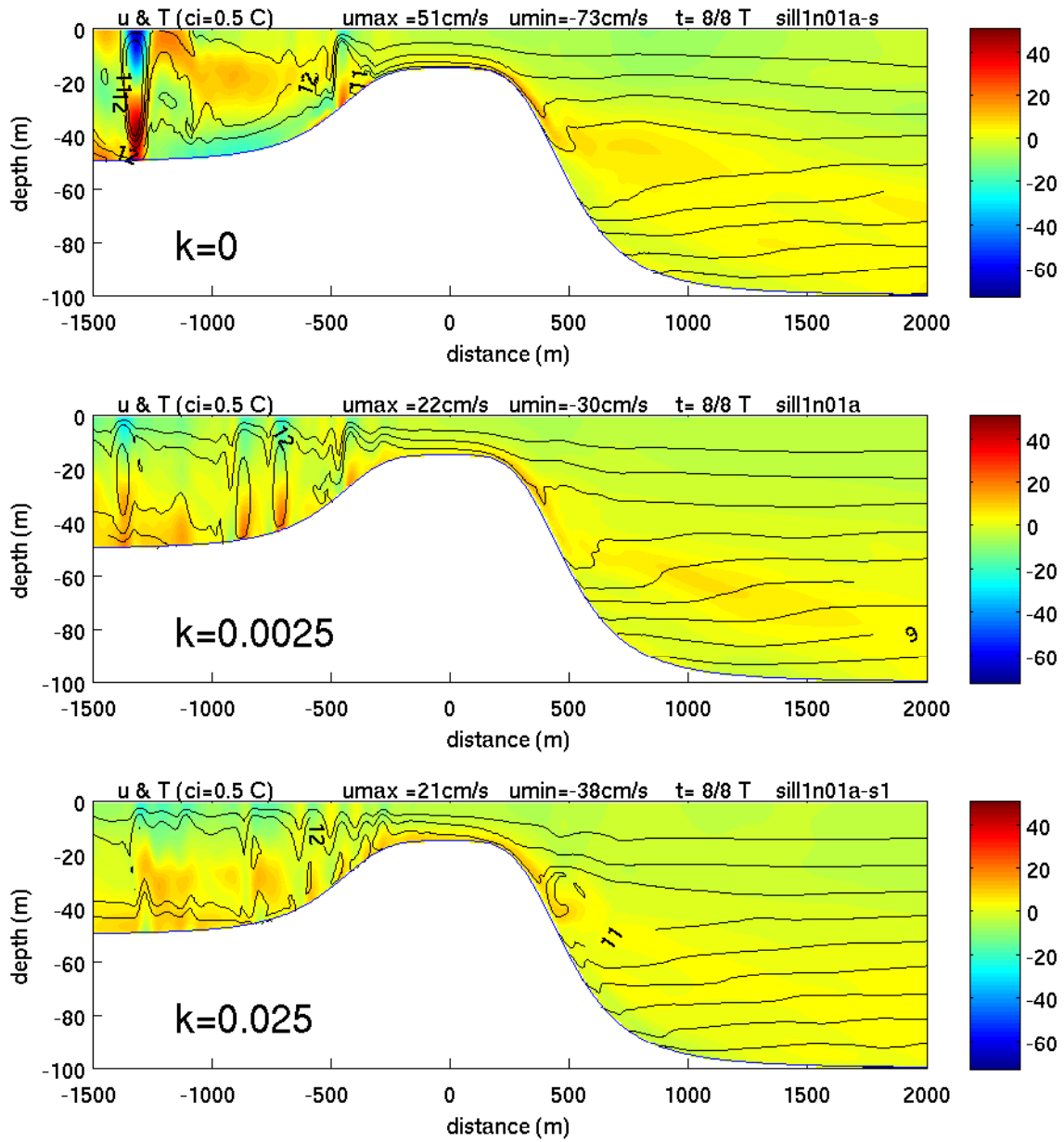


Fig. 2c

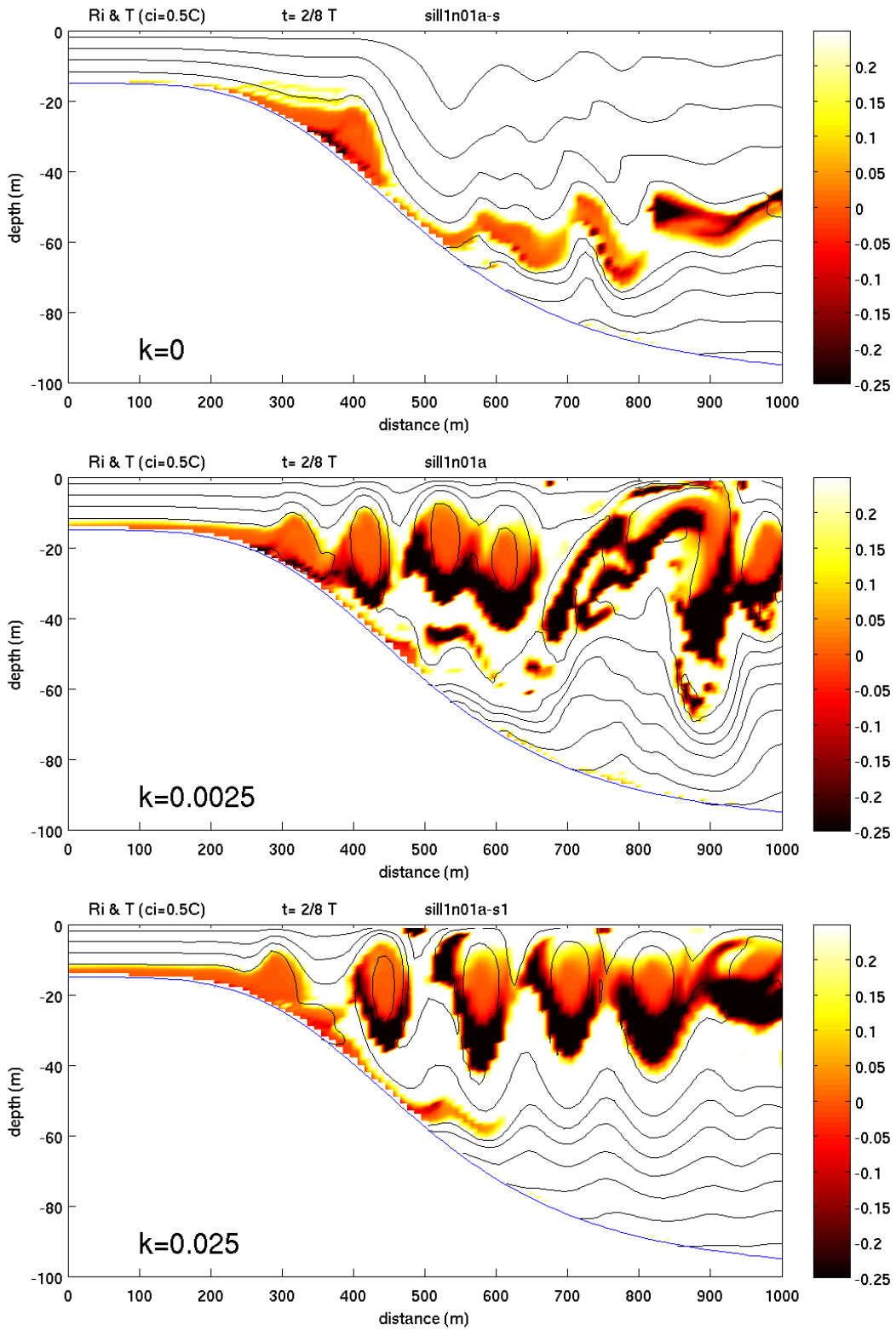


Fig. 3

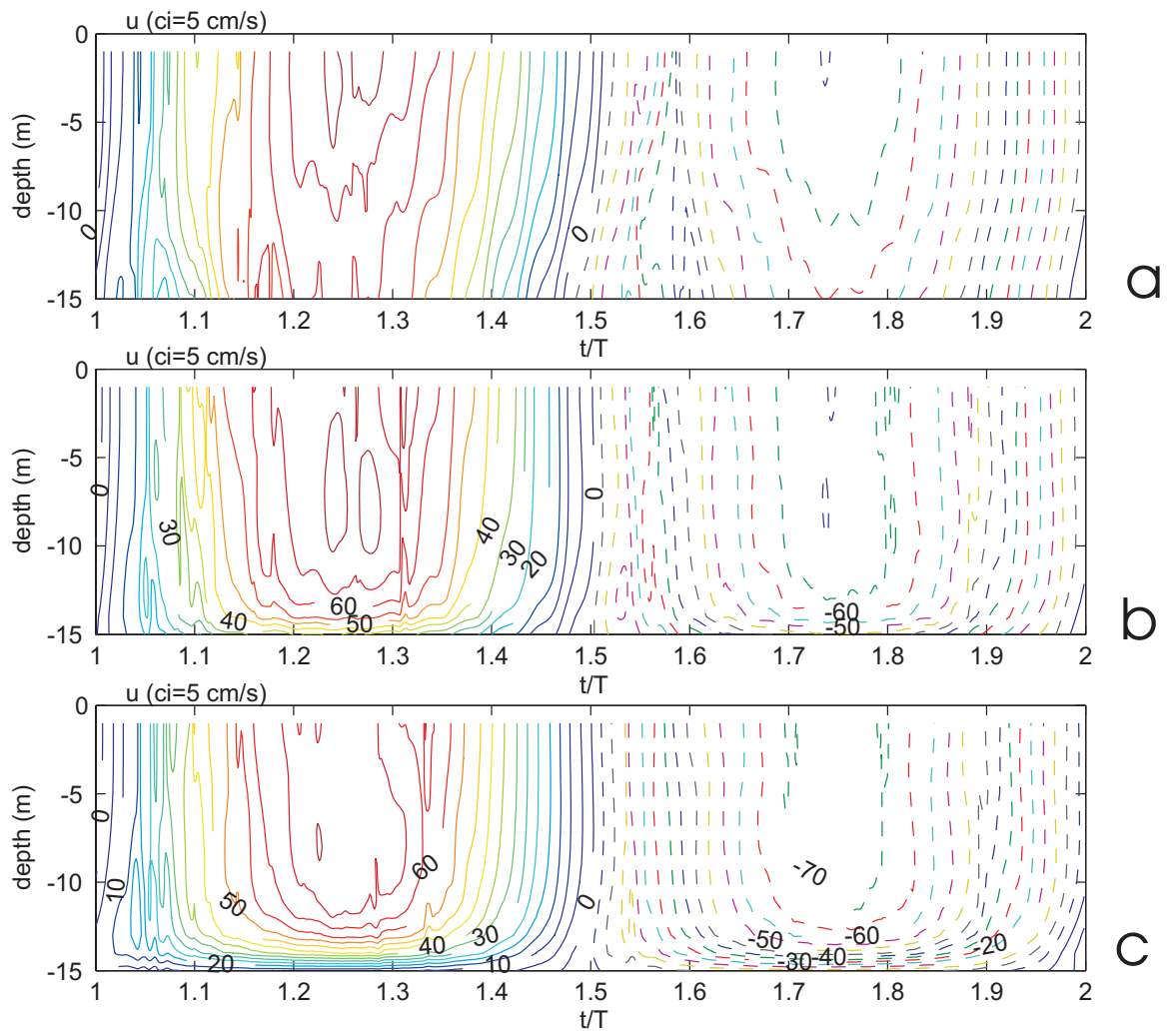


Fig. 4

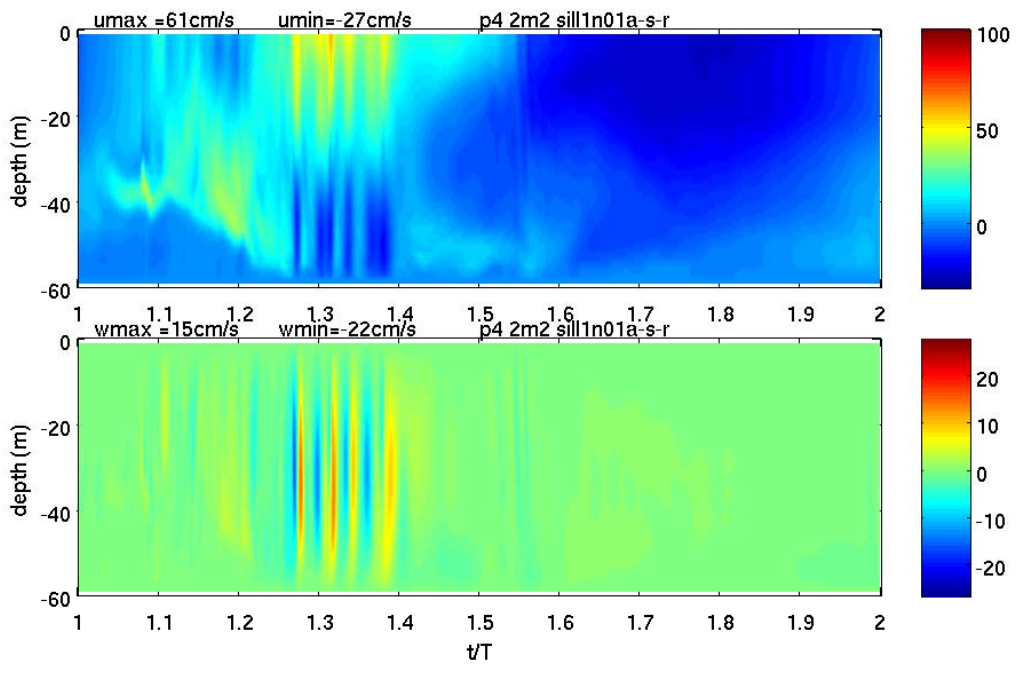


Fig. 5a

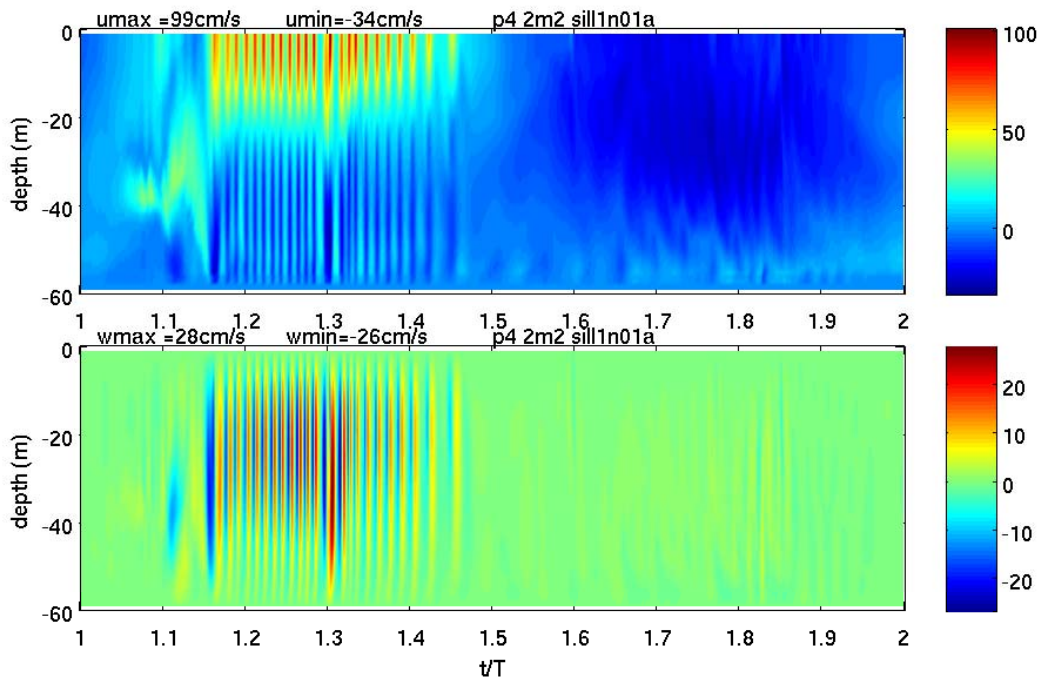


Fig. 5b

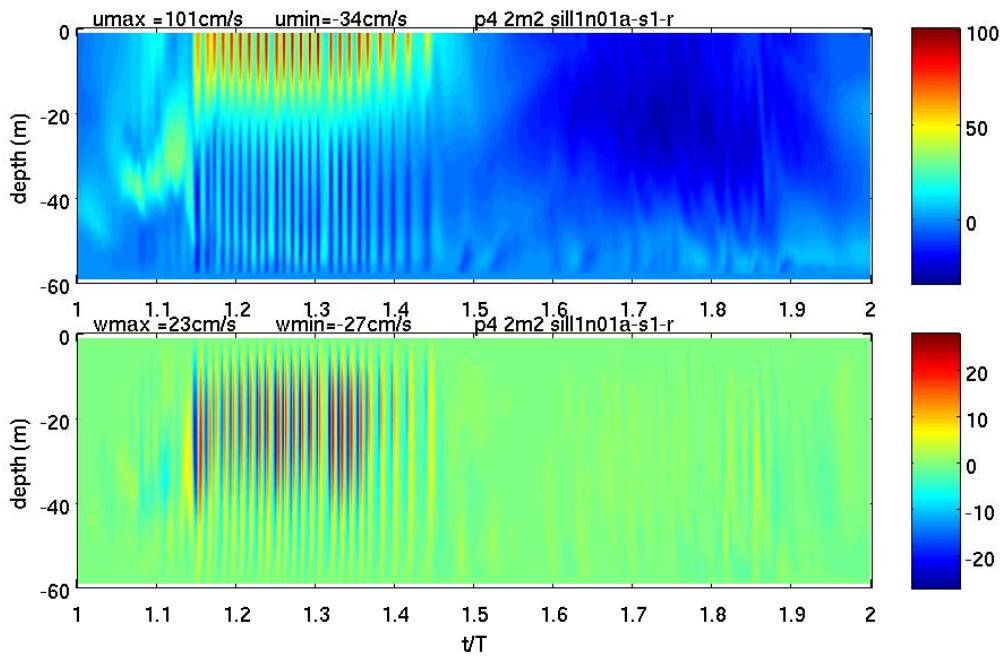


Fig. 5c

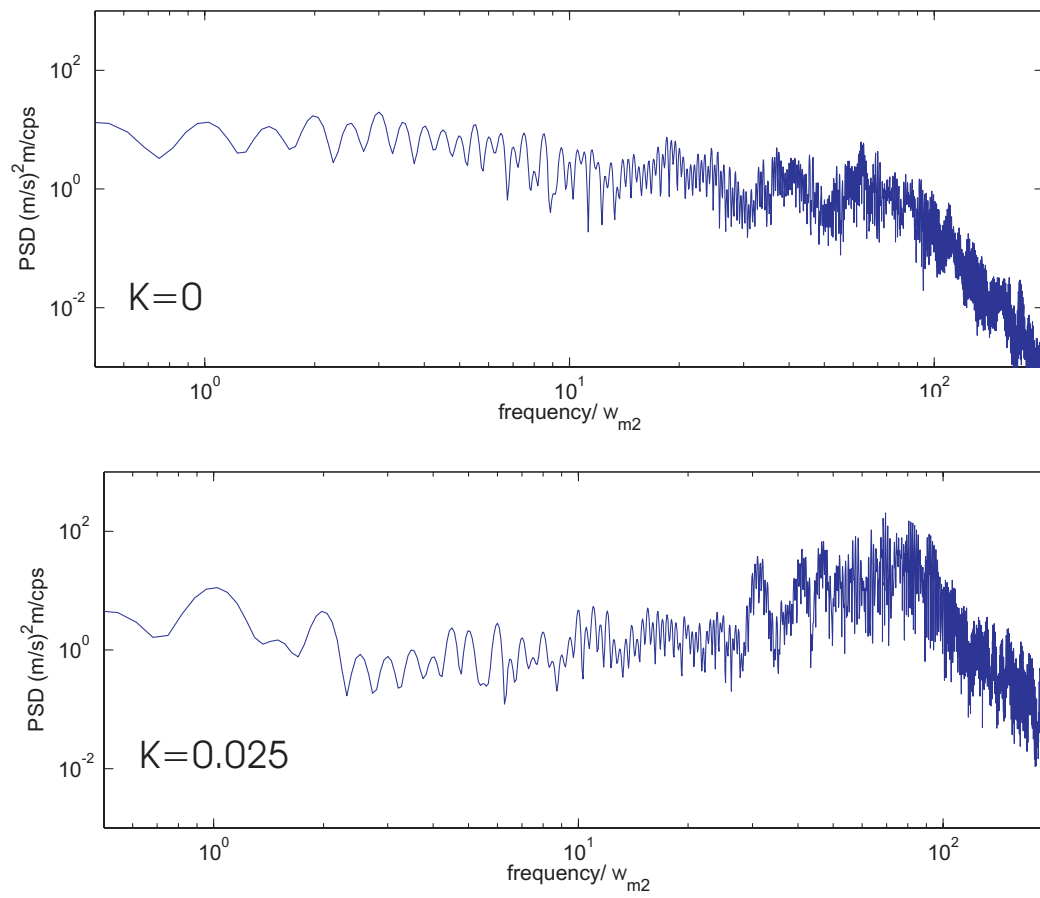


Fig. 6

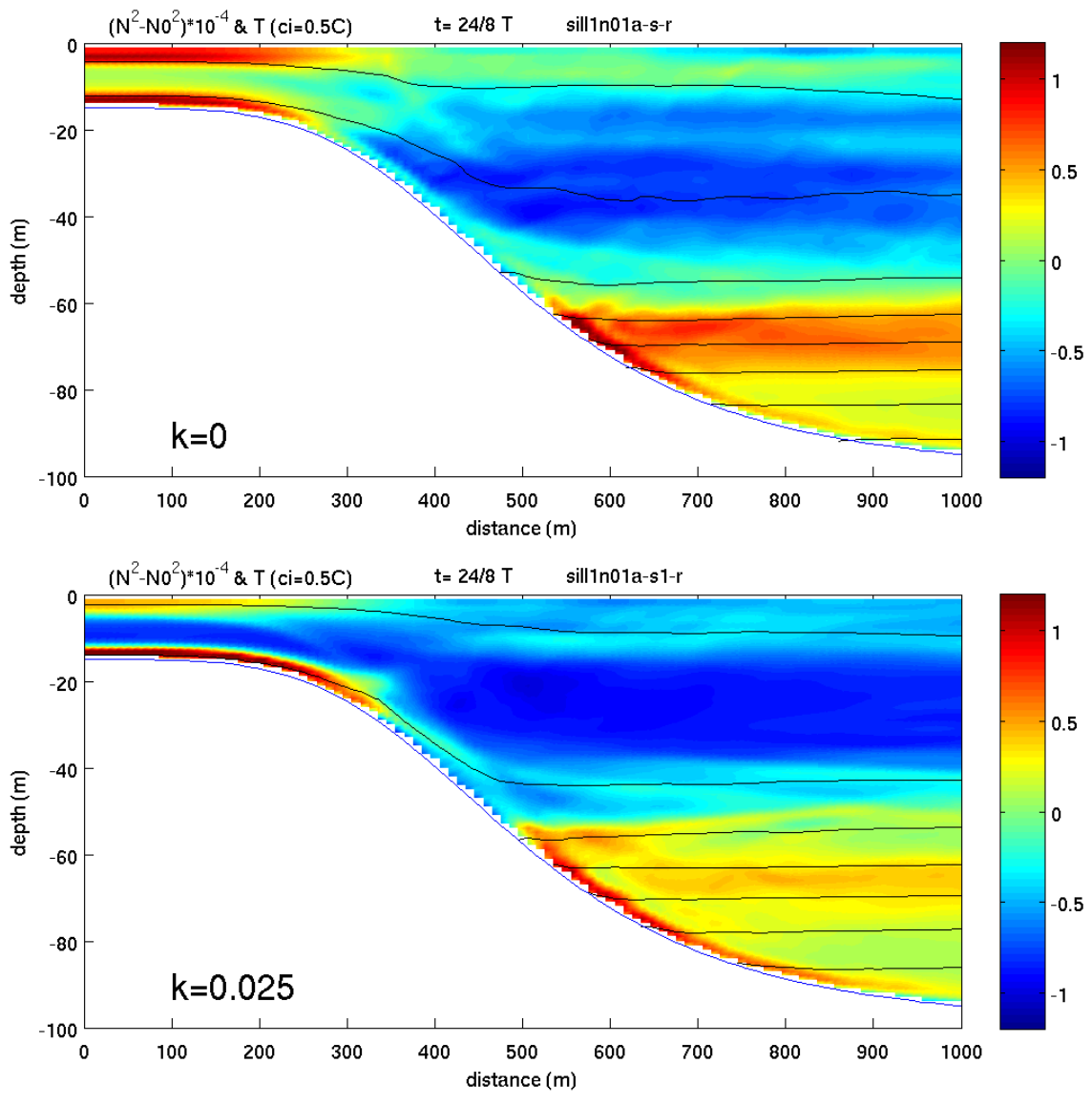


Fig. 7a

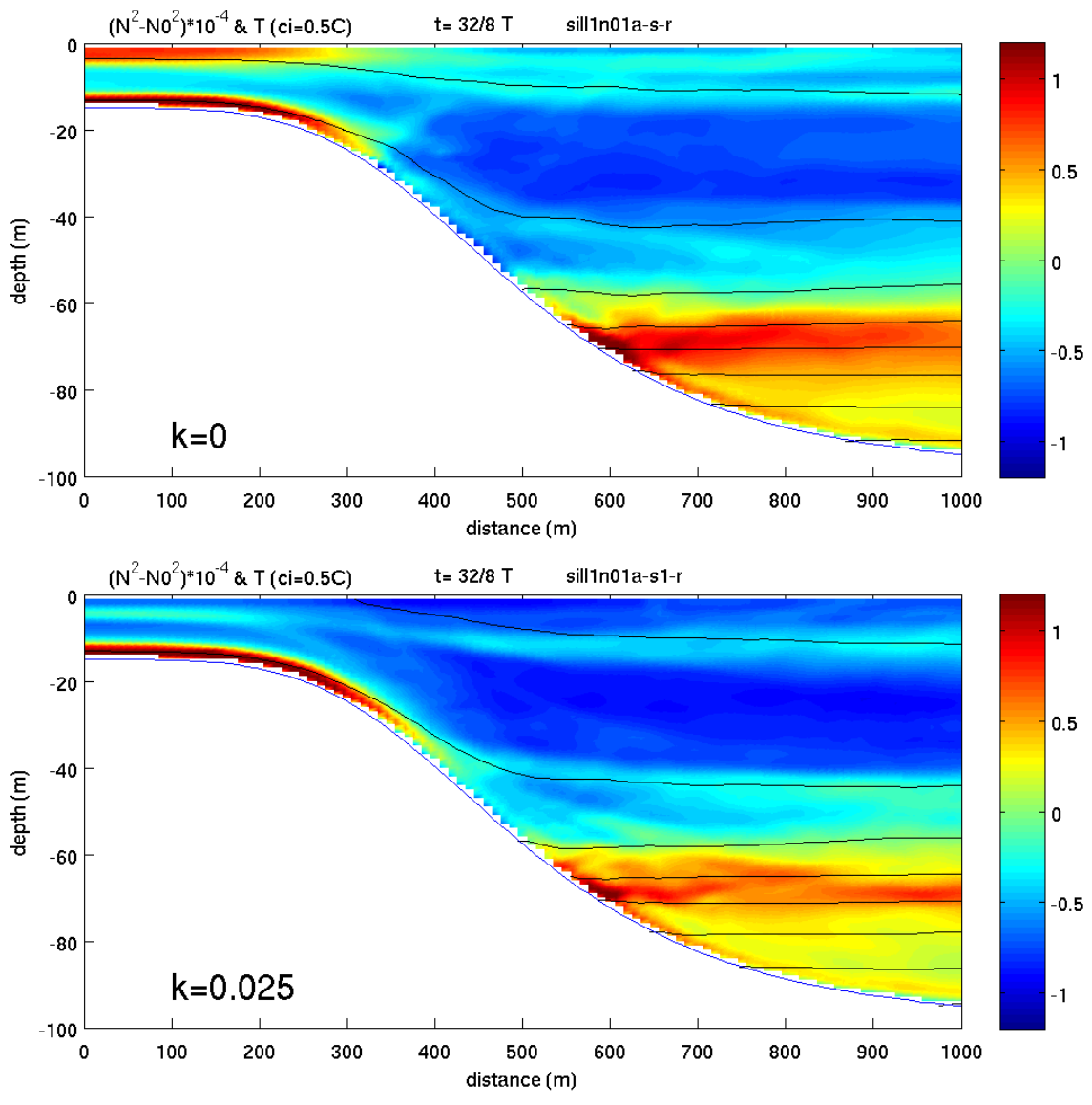


Fig. 7b

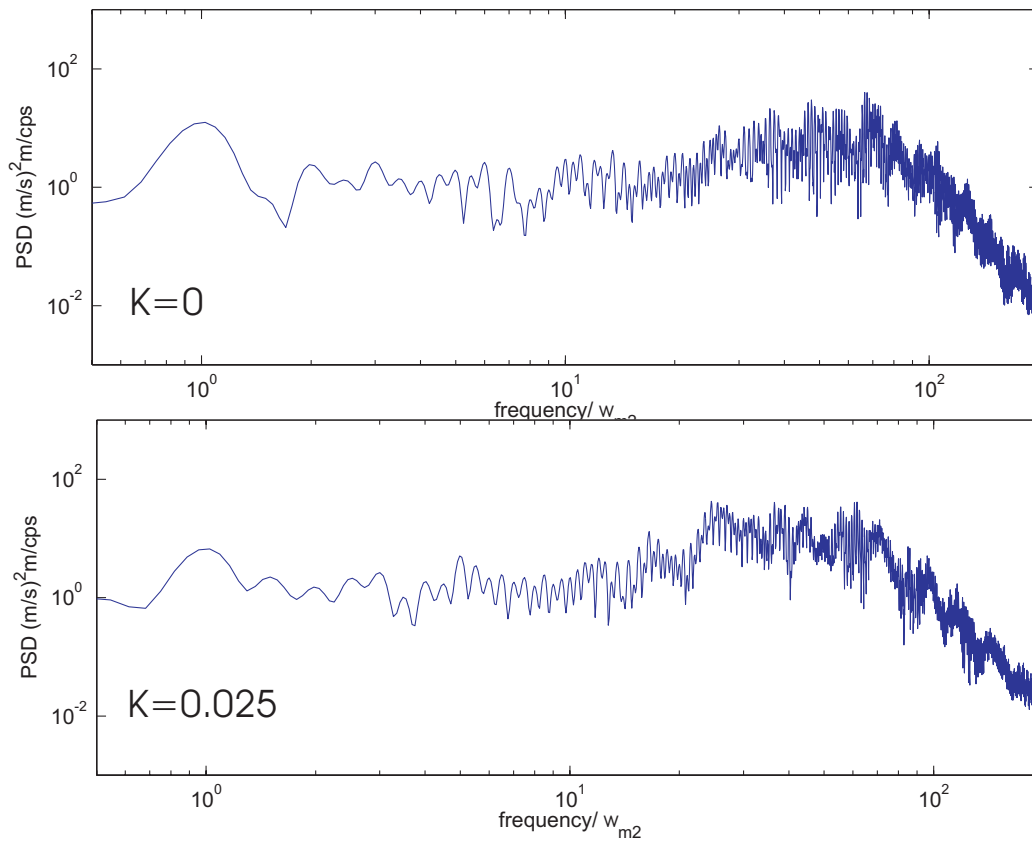


Fig. 8

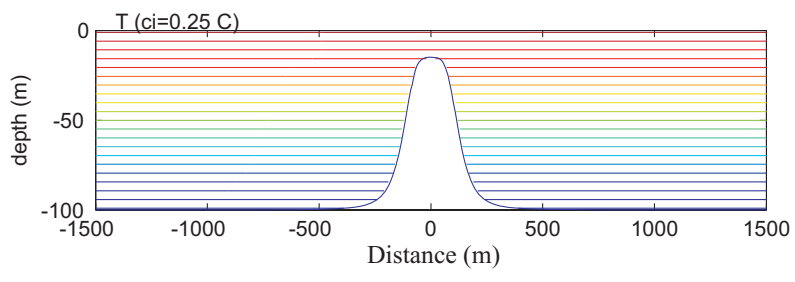


Fig. 9

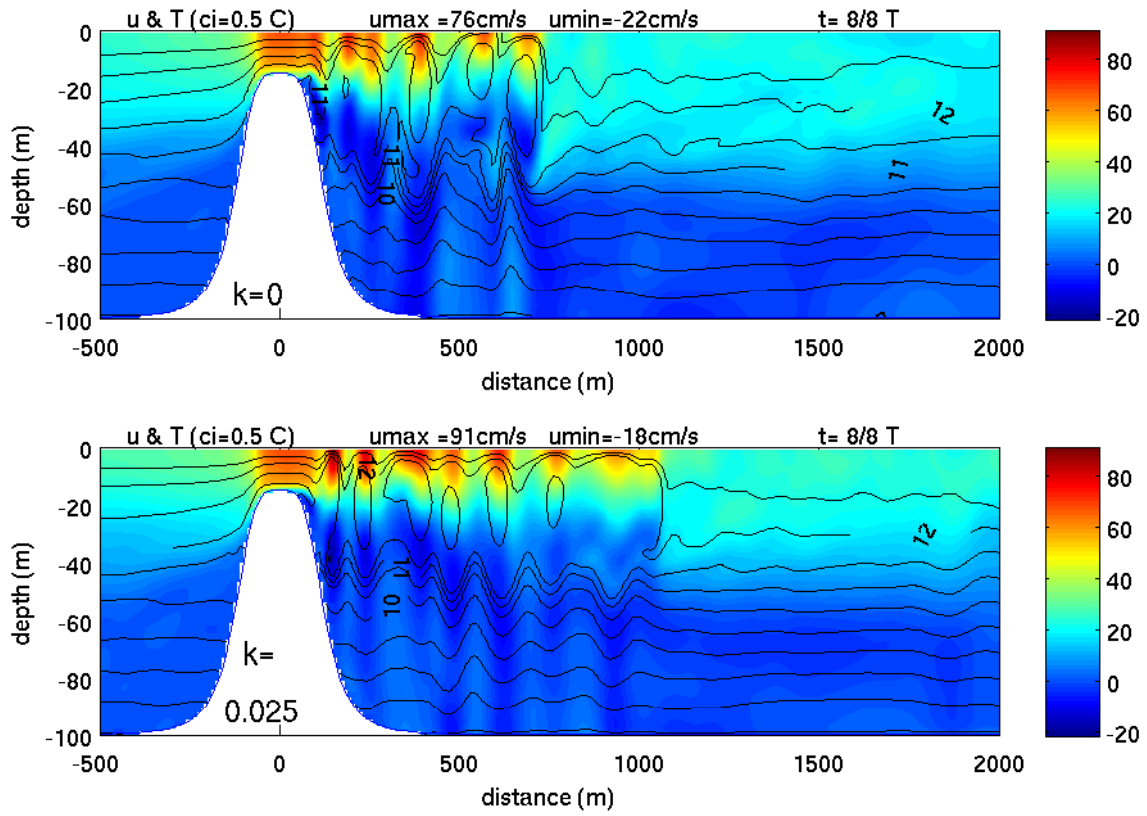


Fig. 10a

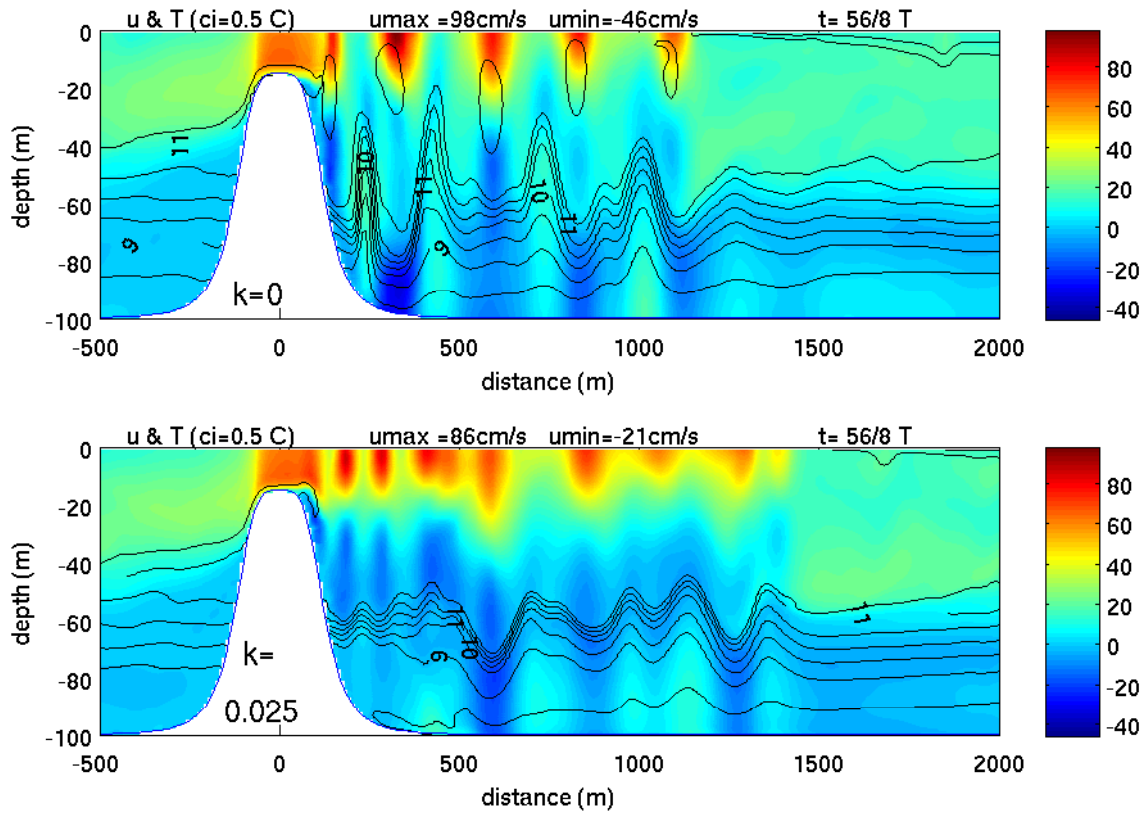


Fig. 10b

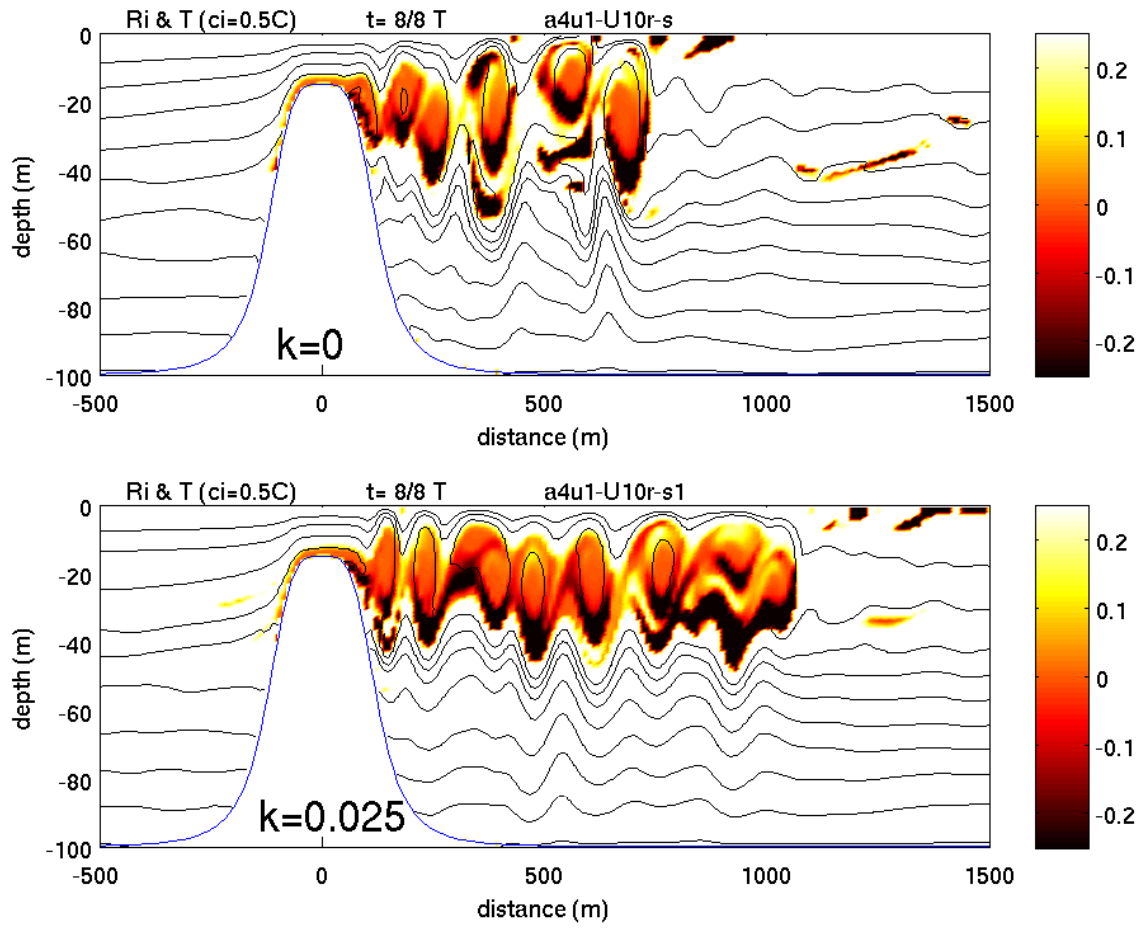


Fig. 11a

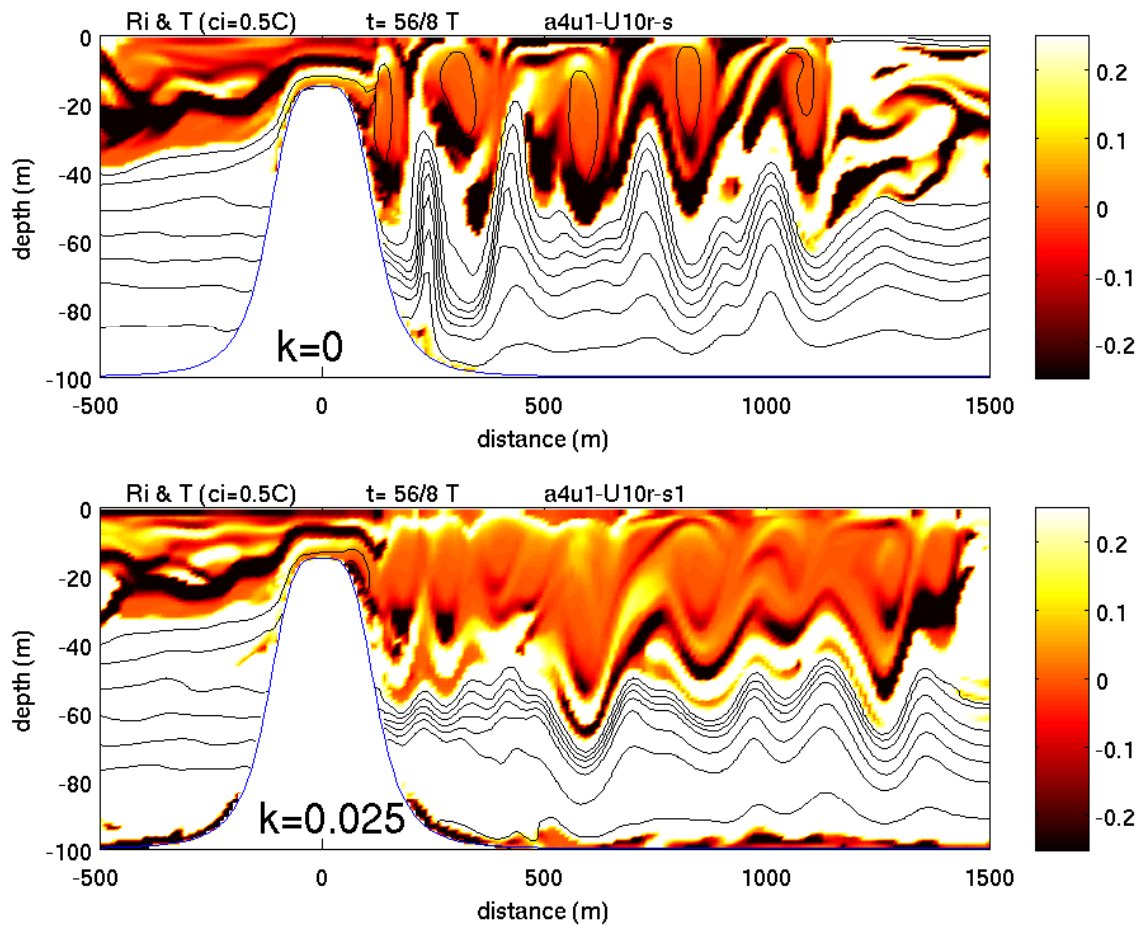


Fig. 11b

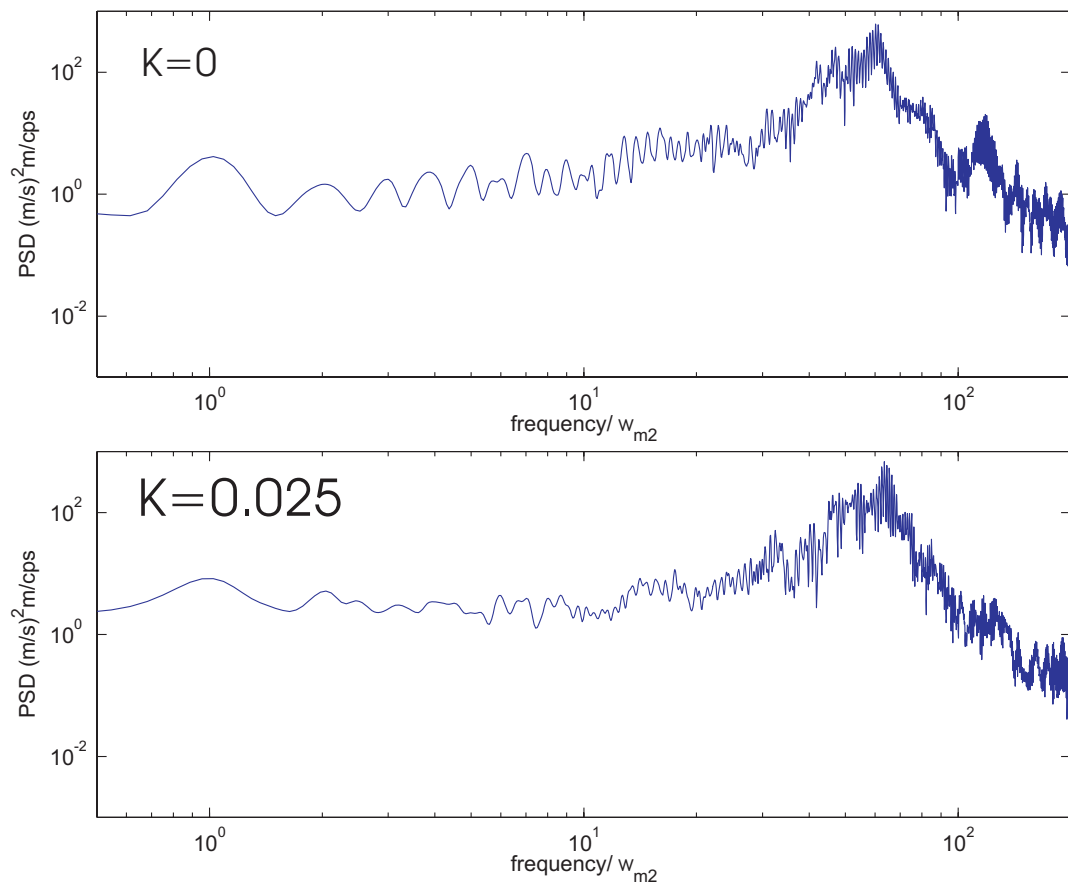


Fig. 12

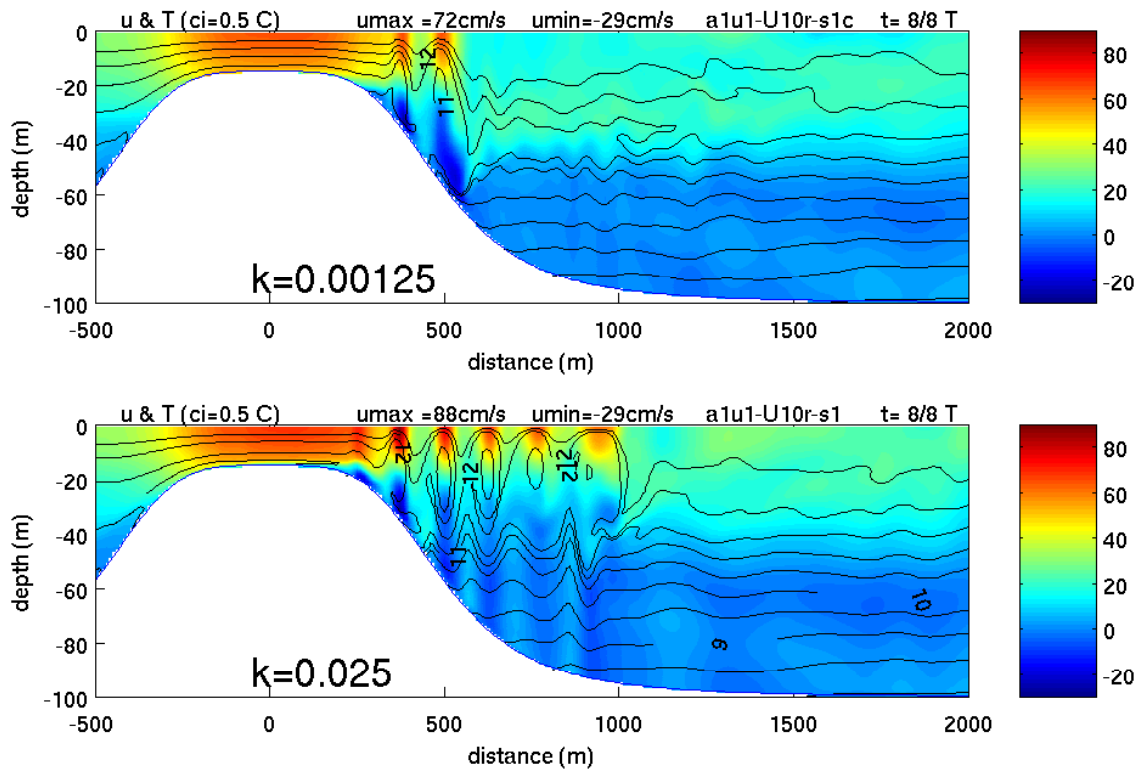


Fig. 13a

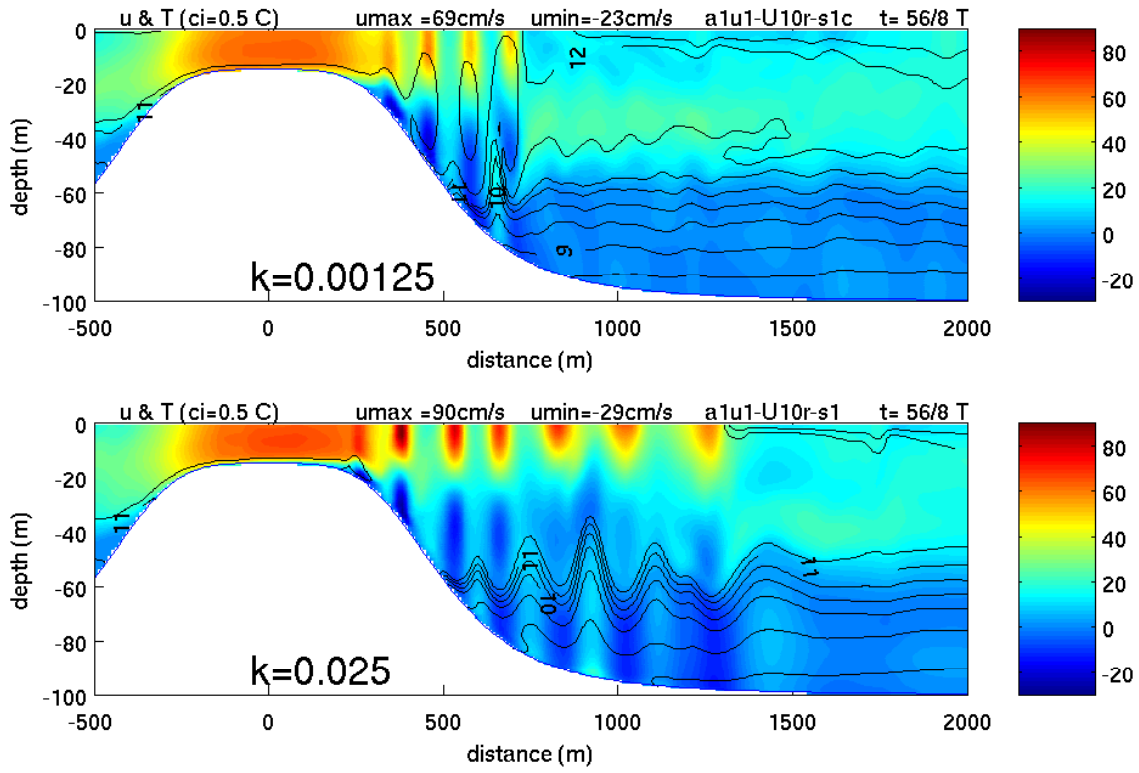


Fig. 13b

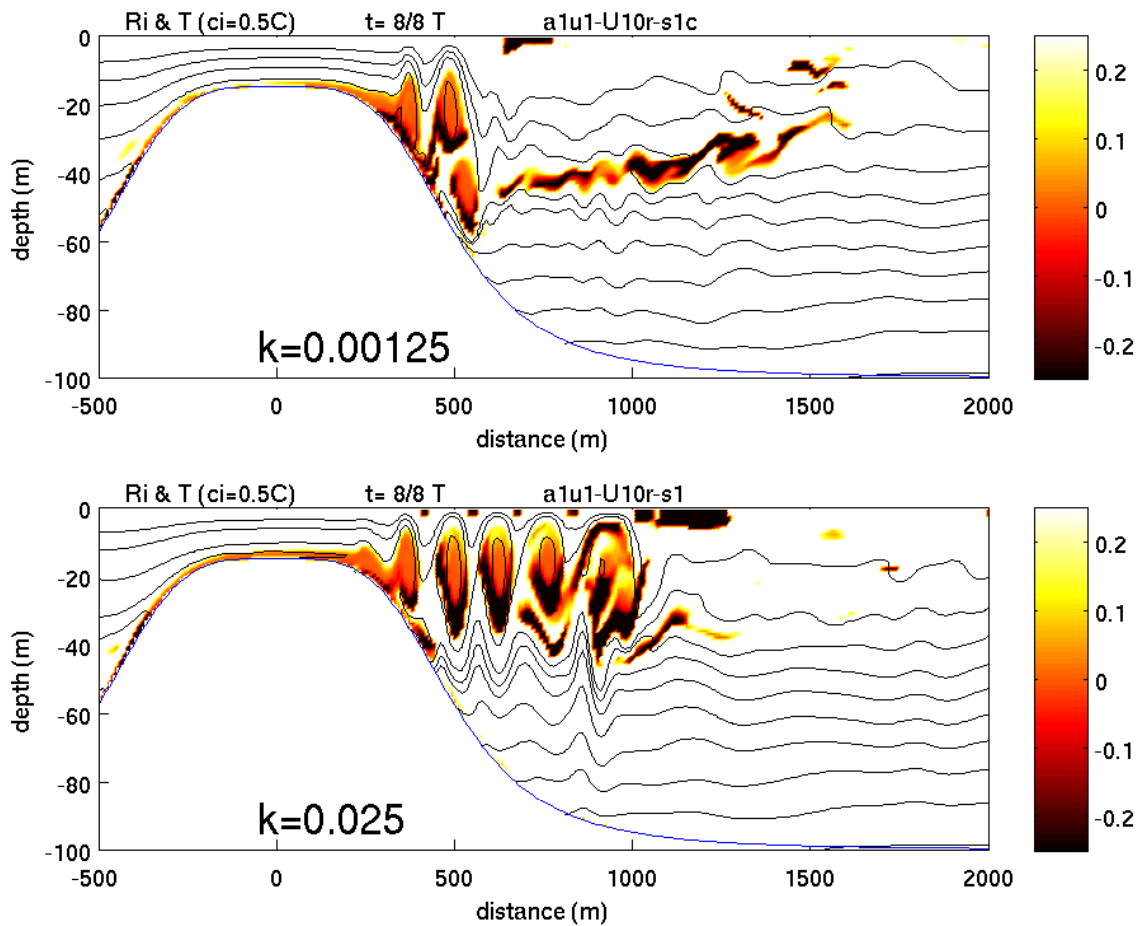


Fig. 14a

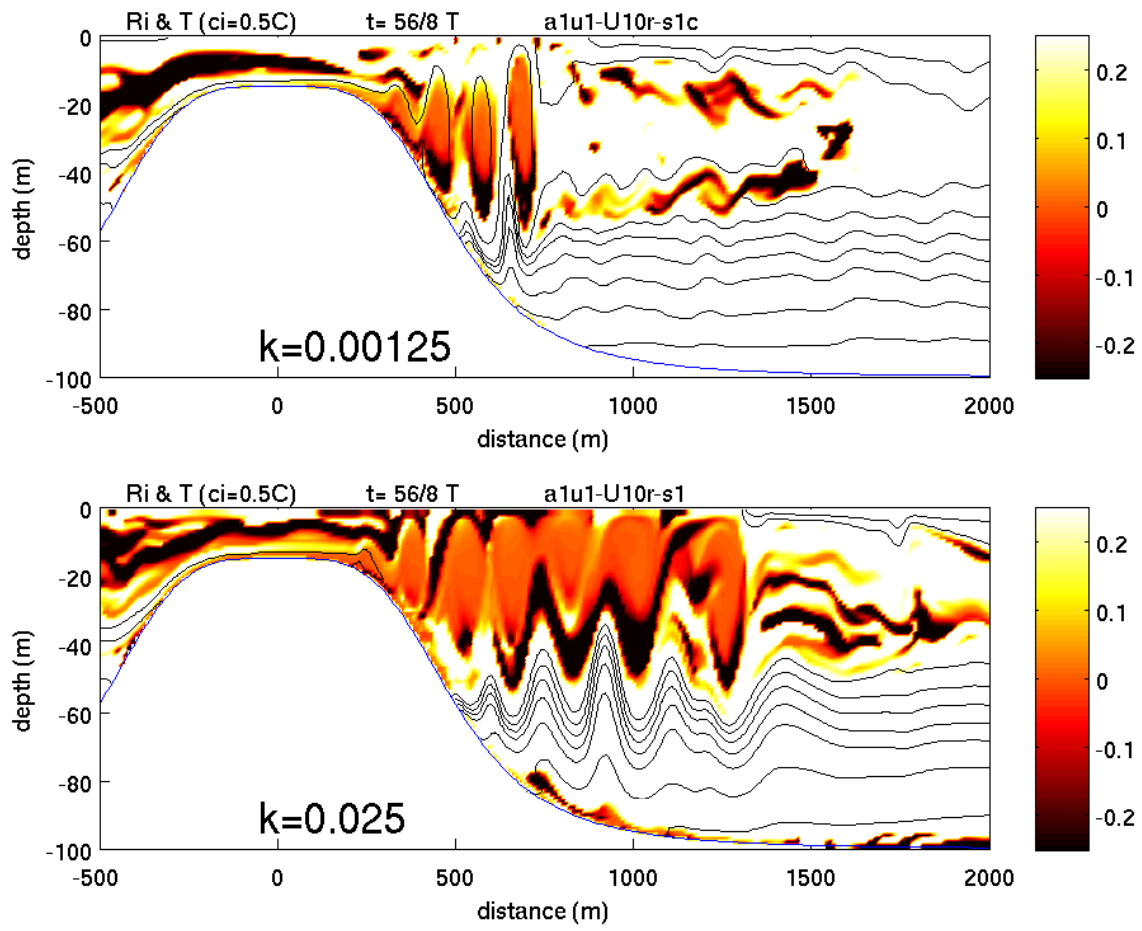


Fig. 14b

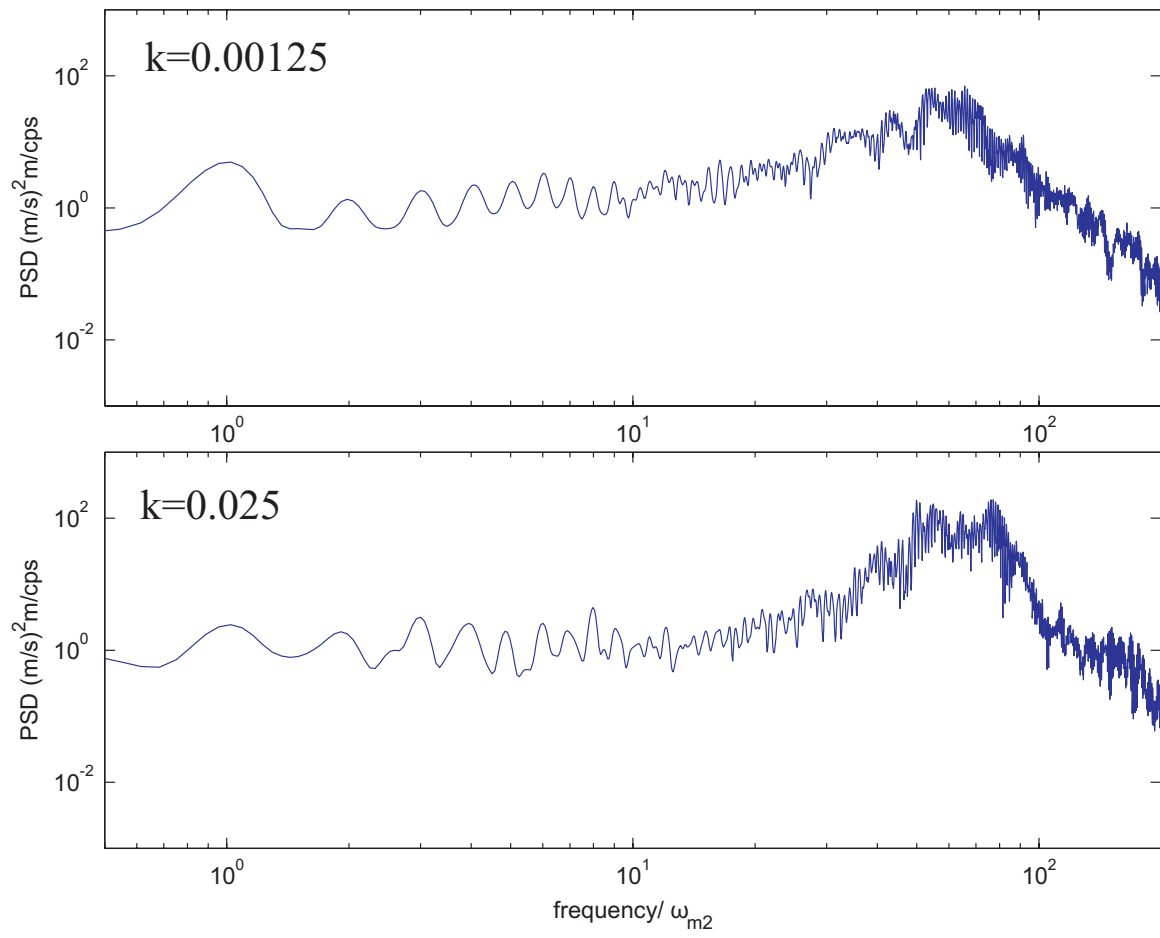


Fig. 15

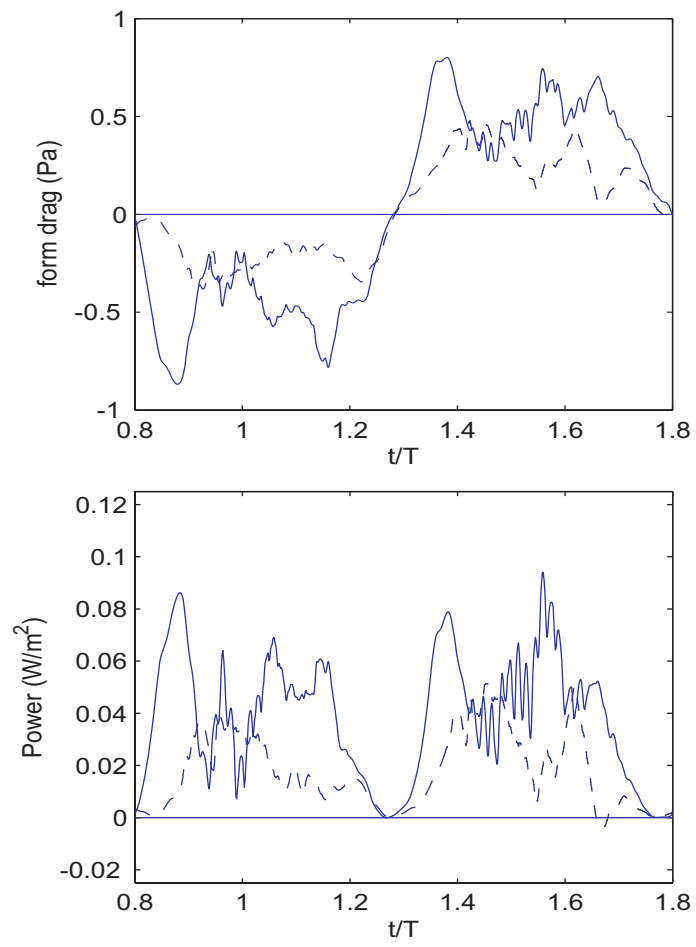


Fig. 16

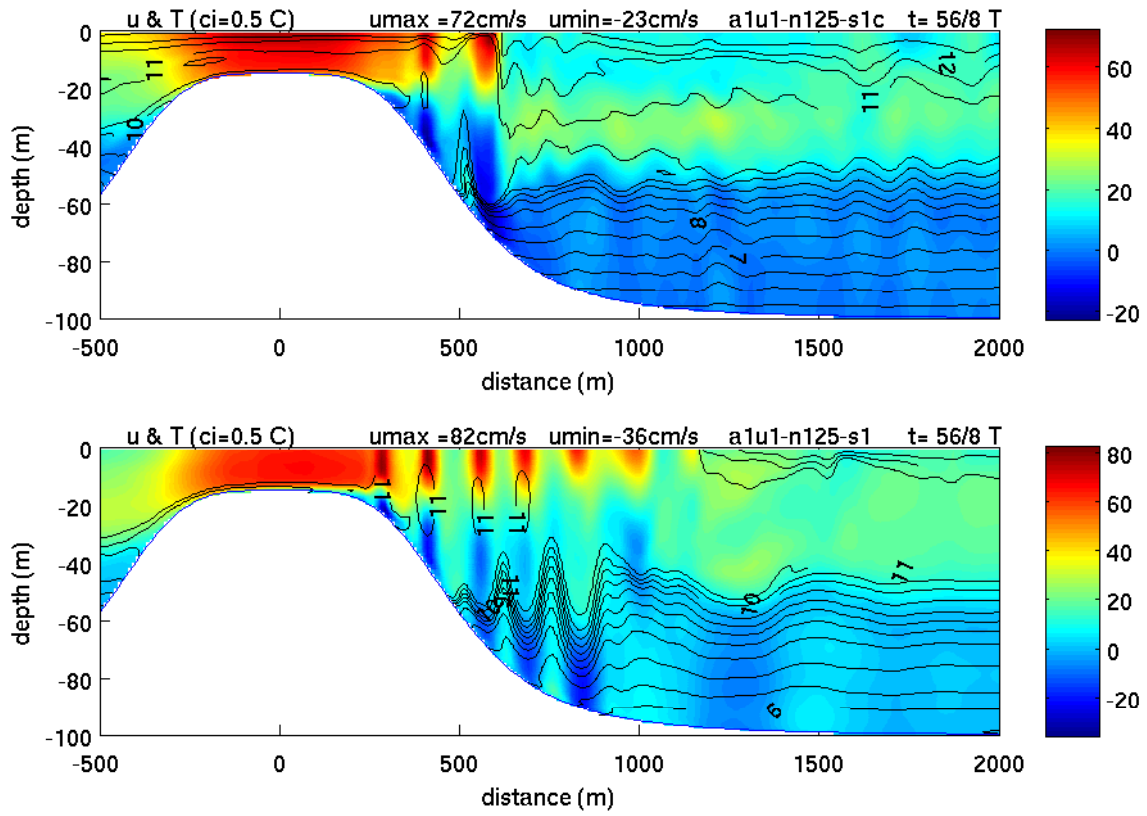


Fig. 17

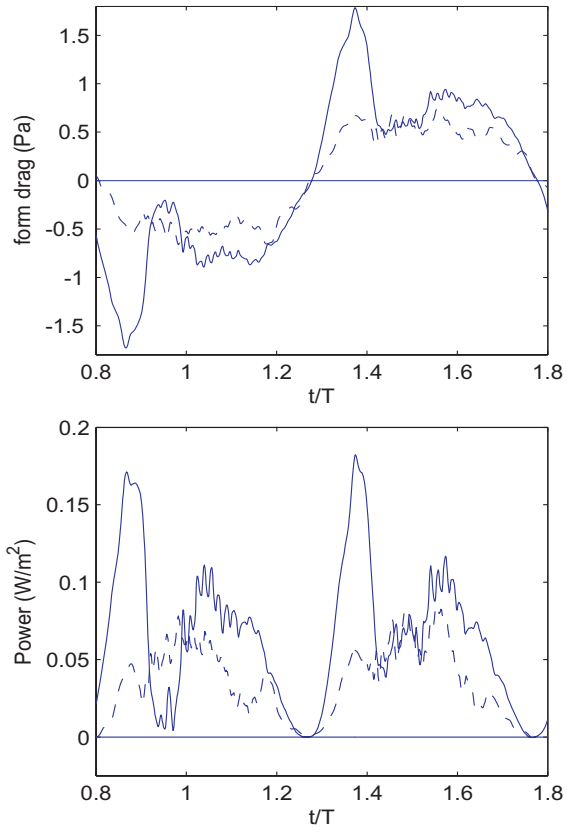


Fig. 18